energies

Article

Simulation-Based Performance and Cost Optimization of Alkaline Electrolyzers

Sami Şaban Demirezen [1], Ahmed Emin Kılıç [1,2], Selahattin Çelik [1,2], Hasan Ozcan [1,2] and Bahman Amini Horri [3,*]

1 Faculty of Engineering and Natural Sciences, Ankara Yıldırım Beyazit University, Ankara 06010, Türkiye
2 Hydrogen Technologies and Energy Research Centre (H2 TEAM), Ankara Yıldırım Beyazit University, Ankara 06010, Türkiye
3 School of Chemistry and Chemical Engineering, University of Surrey, Guildford GU2 7XH, UK
* Correspondence: b.aminihorri@surrey.ac.uk

Abstract

The acceleration of the green energy transition has reinforced the importance of reliable, cost-effective hydrogen production technologies. Alkaline water electrolyzers (AWEs) have become a critical option due to their lack of requirement of platinum group metals, as well as their scalability; however, the materials, geometry, and operating conditions used must be comprehensively evaluated alongside electricity costs. This study presents an approach that directly integrates a COMSOL-based electrochemical polarization model with a techno-economic module and validates the results against published U–J curves and 2024 public LCOH ranges. The scans across the 25 kW–10 MW range show that temperature and separator porosity are the most powerful factors affecting performance; narrow cell gaps significantly reduce ohmic losses, and the electrolyte concentration provides limited additional benefit beyond a certain threshold. KOH outperforms NaOH under most conditions, but the difference between the two electrolytes narrows as temperature increases. Economic analyses confirm that electricity price is the dominant determinant of LCOH; levels of 4–5 $\$\cdot kg^{-1}$ are achievable at the MW scale, while high-cost scenarios reach 7–10 $\$\cdot kg^{-1}$. In conclusion, the study provides a validated and scalable framework for the joint optimization of AWE design and operation.

Keywords: alkaline water electrolysis; techno-economic analysis; polarization modelling; ohmic loss reduction; electrolyzer design optimization; levelized cost of hydrogen (LCOH); zero-gap cell architecture

Academic Editors: Adriano Sacco and Antonino S. Aricò

Received: 14 December 2025
Revised: 12 January 2026
Accepted: 27 January 2026
Published: 4 February 2026

1. Introduction

Global primary energy demand is projected to increase by an average of 1.3 percent annually by 2040, driven by sustainable economic growth, population growth and technological developments [1]. Despite efforts to diversify sources, oil, natural gas and coal are expected to remain dominant in supply until at least 2050 [2]. The intensive use of fossil fuels in energy production and chemical processes accelerates climate change and deepens environmental impacts through CO_2, NO_x, VOC and particulate matter emissions [3]. The increasing demand for fuel and the limited availability of fossil fuels have made the development of clean, environmentally friendly alternatives an urgent necessity [4]. In this context, hydrogen stands out as a strategic option in energy conversion due to its high specific energy content (HHV $\approx$ 39.42 $kWh\cdot kg^{-1}$; $\approx$120 $MJ\cdot kg^{-1}$) and strong integration potential with different sectors [5,6].

 https://doi.org/10.3390/en19030835

Hydrogen production is grouped into two main categories: traditional methods (SMR, naphtha/petroleum reforming and coal gasification) and electrolysis-based methods [7–9]. Fossil fuel-based methods are environmentally disadvantageous due to their high emission profiles [8,9]. In contrast, water electrolysis enables on-site, low-emission production by splitting water into H_2 and O_2 using electrical energy. In recent years, the anion exchange membrane (AEM) approach has been added to the three mature technologies of solid oxide electrolysis (SOE), alkaline water electrolysis (AWE) and proton exchange membrane (PEM) electrolysis [10,11].

Among electrolysis technologies, AWE serves as a rational reference point for research-focused studies due to its maturity level, material availability, and cost base. Operating at approximately 70–90 °C and mostly at atmospheric pressure, AWE cells can produce high-purity hydrogen with KOH electrolytes and nickel-based electrodes that do not require platinum group metals; the typical cell voltages are 1.8–2.4 V and the energy consumption is in the 5–6 $kWh \cdot Nm^{-3}$ range. Thanks to commercial porous separators (e.g., Zirfon-class polysulfone/PPS-based diaphragms) and long-lasting stack architectures, stable operating lifetimes of tens of thousands of hours are achieved, while the stack costs are lower than those of PEM. Although PEM electrolyzers can operate at higher current densities, they rely on expensive noble metal catalysts and ionomer membranes; AEMs still exhibit limited durability and maturity and SOEs are constrained by high temperature and capital requirements. In this context, AWE provides a suitable platform for this study, which targets performance–cost optimization by offering an advantageous foundation in terms of scalability and total cost of ownership [12–16].

Among these studies, AWE offers a cost-effective solution for large-scale hydrogen production with technological maturity, durability, and a material option that does not require platinum group metals [17,18]. A typical AWE cell operates at 60–90 °C and <30 bar conditions, with two Ni-based electrodes separated by a porous separator in an aqueous KOH electrolyte [19]. AWE systems have found applications in a wide range of fields, including energy production, semiconductor and flat panel manufacturing, thermal processing and analytical laboratories; they have also found new uses as an alternative carrier to helium in gas analyzers and as a fuel source in flame detectors [20,21]. The integration of AWE with renewable (PV and wind) sources is particularly important for balancing intermittent production and supplying carbon-free hydrogen [22].

The key factors determining AWE performance are temperature, pressure, electrolyte (KOH) concentration and conductivity, electrode–separator distance, current density, bubble formation/suppression and cell architecture. The literature shows that increasing temperature reduces the reversible voltage, thereby decreasing cell voltage at certain current densities and increasing efficiency; however, in some cases, parasitic currents can limit the Faraday efficiency [23,24]. It has been reported that a KOH concentration range of 30–50% minimizes ohmic losses [23] and that conductivity peaks at 34–38% KOH [25]. Reducing the electrode/separator distance (zero-gap approach) reduces ohmic losses; ~0.4 mm has provided the minimum cell voltage under certain flow conditions [25,26]. Bubble dynamics and electrode surface coverage affect mass transfer, particularly at current densities > 0.1 $A \cdot cm^{-2}$ [27]. Pressure increases can reduce bubble sizes and lower ohmic resistance; however, adverse effects on purity and some efficiency metrics may be observed.

Modelling and experimental studies in the field of AWE have systematized design and operational strategies aimed at performance enhancement. Early-stage dynamic and system-level approaches based on SIMELINT and TRNSYS software (software versions not specified in the cited studies) have enabled the prediction of cell voltage, gas purity, and thermal behavior under variable power feed conditions [28–30]. Experimental–empirical studies have shown that (i) temperature affects hydrogen production and yield (plateauing at approximately 50 °C) [31], (ii) pressure increases can elevate the total energy consumption under certain conditions [32], (iii) safe and agile operation with 74–83% efficiency is achievable under wind–PV conditions [33], (iv) heat losses can be reduced by 50–67% with converter design [34] and (v) model/reality mismatches can be kept at ≈2% in voltage and ≈0.9% in production [35]. Advanced cell architectures and separator selection have reduced cell voltage to the 1.7–2.2 V range [36]; ambient temperature operating scenarios have reported up to 12% increases in voltage efficiency and up to ≈6.3-fold reductions in corrosion. More recent studies have validated the conductivity peak (~94.5 $S{\cdot}m^{-1}$ @ 32% KOH; 50 °C) [37] and quantified parameter effects (T, p, KOH, current density and electrode spacing) using MATLAB/SIMULINK (v7.0) and Aspen Plus (v8.0) [38,39], and reported efficiency in the range of 77–78.6% in PV/wind emulations [40].

Alongside performance, thermoeconomic assessments form the second axis determining AWE competitiveness. It has been reported that hydrogen cost can vary between 3–15 €$\cdot kg^{-1}$ depending on electricity consumption; specific energy consumption is ≈4–7 $kWh{\cdot}Nm^{-3}$, and CapEx ranges from 1000–5000 $\$\cdot kW^{-1}$ depending on capacity [41]. Approaches such as ambient temperature operation can reduce the cost from 13.61 £$\cdot kg^{-1}$ to £11.13$\cdot kg^{-1}$ while reducing electrode corrosion by 2–6 times [42]. Country/region comparisons have detailed investment costs (~990–1020 €$\cdot kW^{-1}$), electricity consumption (≈53.9 $kWh{\cdot}kg^{-1}$) and private/social LCOH metrics [43]. While the typical CapEx for AWE is reported in the range of 600–1200 $\$\cdot kW^{-1}$ and LCOH in the range of 4.5–6 $\$\cdot kg^{-1}$ [44], the learning effect, automation and low/renewable electricity prices have been shown to aggressively reduce costs (to 0.29 $\$\cdot kg^{-1}$ in the best-case scenario) [45]. The CapEx at 100 MW+ scales is projected to stabilize in the 320–400 $\$\cdot kW^{-1}$ range by 2030, consistent with an approximate 25% learning rate [46]. The estimates of 397–940 $\$\cdot kW^{-1}$ and an approximate learning rate of 18.8% for 2030 also support this trend [47]. Current assessments report a CapEx of \$500–1331 per kW_e, OpEx ≈ 2% CapEx and LCOH of 2.09–2.66 $\$\cdot kg^{-1}$ [48]. Reports of 200–360 $kg{\cdot}h^{-1}$ production and 60–82% efficiency (in HHV/LHV terms) with 16–20 MW class systems in industrial applications demonstrate the scalability and maturity of AWE [49–52]. However, the majority of the existing literature either focuses solely on electrochemical performance or bases its techno-economic analyses on empirical coefficients. Most models fail to establish a direct relationship between the internal cell potential distribution and cost components, and therefore cannot explain, on a physical basis, the effects of parameter changes (e.g., temperature, gap distance and electrolyte concentration) on LCOH. Furthermore, approaches that do not include model–experiment comparisons limit the reliability of numerical results. This situation complicates the simultaneous optimization of AWE systems in terms of both performance and cost, and highlights the lack of integrated tools that would provide decision support at the engineering scale.

In recent years, integrated modelling approaches that simultaneously address the technical and economic performance of alkaline electrolyzer systems have become increasingly prevalent. A significant portion of this research represents the electrolyzer stack and balance-of-plant (BoP) systems in process simulation environments such as Aspen Plus, enabling LCOH calculations based on system-level mass–energy balances [53]. However, these approaches often fail to explicitly analyze the sensitivity of the internal cell potential distribution, ionic conduction pathways, and ohmic losses to geometric and material-based parameters. Consequently, the effects of fundamental design variables, such as temperature, electrode–separator distance, separator porosity and electrolyte properties, on LCOH are reflected indirectly through empirical coefficients rather than physical principles. This study aims to establish a parametric and traceable performance–cost relationship by presenting a framework that directly translates physically resolved electrochemical outputs at the cell level (polarization curves and ohmic losses) into technical–economic calculations. Throughout this study, the term electrode–separator distance is used to describe the ionic transport path length between the electrode surface and the separator.

In the literature, there are a limited number of integrated modelling approaches that address the performance and cost behaviour of alkaline water electrolyzers together. A significant portion of these studies have derived mass–energy balances at the system level by representing the electrolyzer stack and balance-of-plant (BoP) together in process simulation environments such as Aspen Plus; they then aimed to arrive at indicators such as LCOH using cost functions or economic analysis modules [54]. Similarly, recent studies have reported examples where Aspen Plus-based setups, combined with tools like Aspen Economic Analyzer, have been used to produce technical–economic results based on equipment costs and scaling effects [55]. However, a common limitation of existing approaches is that the performance–cost relationship is mostly established at the system level, and the sensitivity of physical processes such as intra-cell ionic transport/potential distribution to design variables such as electrode–separator distance, separator porosity and electrolyte properties is often not directly addressed. This study aims to establish a consistent and parametric link from performance parameters to LCOH by directly transferring physically resolved electrochemical outputs at the cell level into a technical–economic framework.

This study presents an integrated and reusable framework that combines simulation-based performance analysis with techno-economic optimization for alkaline water electrolyzers. COMSOL-based polarization curves and parametric analysis results (temperature, electrode–separator gap, separator porosity, electrolyte concentration and type) were matched with the cost model developed in the EES environment and examined within the scope of cell/stack geometry and operating window. CapEx–OpEx separation and LCOH calculations were supported by module- and system-scale factors derived from supplier data, providing a numerical, fast and portable tool for reliable cost estimation and design decisions across scales. The novelty lies in coupling a parametrically validated COMSOL electrochemical model with a modular EES cost model, enabling the scale-dependent optimization of AWE systems across both performance and economics. This study aims to address these shortcomings in existing approaches. The COMSOL-based physical polarization model has been tested against validated experimental data, and the results obtained have been directly integrated into the techno-economic calculation module. Thus, performance, cost and energy efficiency across different scales have been correlated within a single framework, resulting in the development of a reliable, transparent and scalable decision support tool for engineering applications. In this respect, the study eliminates the classical distinction in the literature (performance vs. economy) methodologically and provides a holistic perspective on AWE optimization. Table 1 clarifies the novelty and significance of the proposed framework by summarizing, in a comparative manner, the limitations of standard approaches in the literature and how this study addresses them.

Table 1. The limitations of existing AWE models in the literature and the innovative contributions of this study.

Approach	Common Limits in the Literature	Contribution of This Study
Empirical/semi-empirical techno-economic models	Not physically based; no connection to U–J curve data	Electrochemical model directly integrated into LCOH calculation
Only electrochemical simulations	Economic effects and scale changes are not taken into account	Parametric performance data is combined with the cost model
Unverified models in the literature	No experimental comparison is made; reliability is low	The model is verified with published U–J curves and LCOH bands

2. Methods and Modelling

In this study, a two-stage modelling approach was developed to investigate the performance–cost relationship of alkaline water electrolyzers. In the first stage, an electrochemical model was created to determine the potential distribution, current density, and overpotential components at the cell level; in the second stage, the results obtained were correlated with cost and scale factors to calculate the levelled hydrogen cost (LCOH).

The electrochemical model addresses the three fundamental physical processes in alkaline water electrolysis—thermodynamic equilibrium (Nernst equation), charge transfer kinetics (Butler–Volmer equation) and ohmic resistance (Ohm's law)—within the same framework. These expressions are in the standard forms commonly known in the literature [56], and only the main principles have been retained here.

In this study, ohmic overpotential has been addressed within the framework of the classical series resistance approach, but it has been explicitly related to physically meaningful design and operating parameters. Accordingly, ohmic overpotential has been defined by the following expression:

$$\eta_{ohm} = i \cdot R_{ohm} \tag{1}$$

Here, R_{ohm} represents the total ionic resistance contribution in the electrolyte–separator region. It should be noted that Equation (1) is not a fitted empirical correlation but a physically derived expression based on Ohm's law; therefore, no regression coefficients or fitting metrics such as R^2 are applicable at the equation level. In this study, R_{ohm} is expressed as a function of the electrode–separator gap and the effective ionic conductivity of the electrolyte/separator medium:

$$R_{ohm} = d/\sigma_{eff}(T, C, \varepsilon, \tau, t_{sep}) \tag{2}$$

In Equation (2), d denotes the electrode–separator distance, while σ_{eff} represents the effective ionic conductivity, which depends on temperature (T), electrolyte concentration (C) and the structural properties of the separator (separator porosity ε, tortuosity τ and thickness t_{sep}). The intrinsic conductivity of the electrolyte, which depends on temperature and concentration, has been obtained from empirical relationships reported in the literature, and the necessary density–concentration conversions are provided in the Appendix A for standardization purposes. This parametric expression reveals how electrochemical design and operating parameters (d, ε, T and C) shape the polarization behaviour through ohmic losses, and enables these effects to be incorporated into LCOH calculations via an integrated technical–economic model.

The polarization expression used in this study is based on the classical series connection approach of resistors, which is widely used in the literature. The formulation proposed here aims to express the fundamental components determining the ohmic overpotential (electrode–separator distance and effective ionic conductivity) in a clear and parametric manner, rather than defining a new physical mechanism. Thus, design and operating variables such as temperature, electrolyte concentration and separator microstructure have been incorporated into the model through direct and physically meaningful parameters. This approach preserves the classical Ohmic law framework while enabling the consistent transfer of performance outputs to economic analyses.

The ionic conductivity of KOH and NaOH solutions as a function of temperature and concentration has been obtained from empirical correlations defined in the literature [57,58]. Density–concentration conversions and intermediate formulae are provided in Appendix A for standardization purposes.

The model was solved in COMSOL Multiphysics 6.1 software using the Secondary Current Distribution approach. The charge transfer at the electrode–electrolyte interfaces

https://doi.org/10.3390/en19030835

was calculated using Butler–Volmer kinetics, the equilibrium potentials using the Nernst equation, and the current density distribution using the field equations of Ohm's law. This method physically demonstrates the effect of temperature and electrolyte conditions on cell voltage. This approach is a quasi-empirical framework that combines mechanistic (physical) modelling with empirical generalizations. A multi-physics model derived purely from first principles is not preferred here due to solution complexity and data requirements; instead, a reduced formulation based on Butler–Volmer and Ohm's law is calibrated with parameters consistent with experimental observations, balancing accuracy and simplicity in terms of engineering calculations. In this model, the equilibrium potential is typically calculated using the Nernst equation in Equation (8).

$$E = E^{\circ} + (RT/nF) \cdot \ln([Ox]/[Red]) \tag{3}$$

where E is the equilibrium potential, E° the standard electrode potential, n is the number of electrons transferred in the reaction, and [Ox] and [Red] represent the concentrations of the oxidized and reduced species, respectively. This equation provides equilibrium conditions in terms of concentrations for electrode reactions and is often used in conjunction with Butler–Volmer kinetics.

The electrolyzer cell was modelled in two dimensions (2D) on COMSOL Multiphysics 6.1. The geometry was deliberately simplified to ensure the consistent and traceable application of boundary conditions. As shown in Figure 1, the active surfaces of the electrodes are defined as boundaries (4) and (8), and the hydrogen and oxygen compartments are separated by a rectangular separator (2, 6, 9, and 10). In the model representation, the electrodes are represented by linear boundaries, the separator by a rectangular area and each flow compartment by two rectangles. The lower and upper boundaries are assigned as electrolyte inlets (1 and 3) and two-phase mixture outlets (5 and 7), respectively. As the electron flow (e^-) moves from the cathode (8) to the anode (4) through the external circuit, hydroxide ions (OH^-) are transported from the anode to the cathode through the separator (9–10). The electrical boundary conditions follow: cathode active surface (8) reference potential V = 0, anode active surface (4) applied cell potential $V = U_{cell}$ (alternatively constant current J = const.) and variables T, Cel, ε, and δ_{sep} are labelled in the relevant regions. The main parameters used in the model and their value ranges are summarized in Table 2.

In this study, COMSOL Multiphysics was chosen because the Secondary Current Distribution interface allows conductivity to be defined using analytical functions dependent on temperature and concentration, enables parametric scans (T, C, porosity, distance and J) to be run in a single session and automatically applies current continuity between geometry layers. Additionally, it provides stable solver options for ill-conditioned linear systems arising at high current densities and easy reproducibility for cross-validation. This integrity is critical for the consistent coupling of the electrochemical model with the techno-economic module.

Boundary conditions have been applied in accordance with Figure 1: the cathode active surface (8) has been assumed as the reference potential with V = 0 and two operating modes have been used for the anode active surface (4): (i) the voltage-controlled mode with $V = U_{cell}$ (Dirichlet) and (ii) the current-controlled mode with $n \cdot i = J_{set}$ (Neumann). The upper boundaries (5 and 7) are electrically no-flux ($n \cdot i = 0$) boundaries; the lower boundaries (1 and 3) are enclosing boundaries and are also electrically $n \cdot i = 0$ (hydraulic transport is outside the scope of this work). The separator region (2, 6, 9 and 10) is modelled as a separate domain, with conditions for potential continuity and normal current continuity applied at the separator–electrolyte interfaces. The effective conductivity $\sigma_{eff} = \sigma \cdot \varepsilon^n$ is defined; δ_{sep}, ε, T, and Cel are assigned as field variables in the relevant regions. This setup provides a seamless transition from analytical equations (ohmic loss expansion and total

U_{cell} decomposition) to numerical solutions, ensuring consistent results across different operating modes.

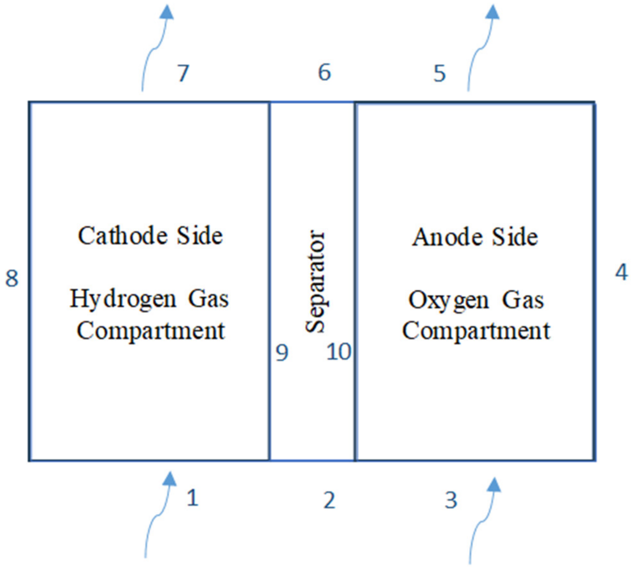

Figure 1. Schematic view of electrolysis cell. The numbers indicate the main cell components and flow ports: (1, 3) electrolyte/reactant inlets, (5, 7) gas outlets, (2, 6) bottom and top manifolds, (4) anode-side compartment wall, (8) cathode-side compartment wall, and (9, 10) separator boundaries. The arrows indicate the inlet flow of electrolyte/water at the bottom of the cell (1–3) and the outlet flow of produced hydrogen and oxygen gases at the top of the cell (7–5).

Table 2. Parameters for COMSOL.

Parameter	Value	Unit
Cathode Side Electrode–Separator Distance Range	2–4	mm
Anode Side Electrode–Separator Distance Range	2–4	mm
Separator Width	1	mm
Cell Height	10	mm
Operating Temperature Range	25–75	°C
Exchange Current Density for Anode Side	100	$A \cdot m^2$
Exchange Current Density for Cathode Side	1	$A \cdot m^2$
Separator Porosity	0.3–0.4	-
Electrolyte Concentration	6–10	mol/L
Electrolyte Solution	KOH-NaOH	-
Operating Voltage Range	1.2–2.4	V

To simplify the model and focus on the major determinants of the electrolysis process, a set of assumptions has been adopted that reduces the computational cost and enhances the model's physical interpretation. This framework facilitates the decomposition of parameter effects, improves numerical stability, and enables the consistent execution of comparative scenario analyses.

Some assumptions were applied: (i) the working fluids are assumed to be Newtonian, viscous and incompressible; (ii) the physical properties, including density and conductivity, are assumed constant throughout the solution; (iii) the electrolyte is assumed to be spatially uniform, as the influence of ion distribution on macroscale responses is considered limited; (iv) the flow is modelled as isothermal and, hence, the heat transfer/energy equations are omitted from the solution set; (v) surface tension effects are negligible; (vi) hydrogen/oxygen transfer through the separator is neglected; and (vii) the gas phase volume fraction within the electrolyte volume has been neglected. Assumption (vii) posits that the hydrogen and oxygen gas bubbles produced are instantly and efficiently removed from the electrode surface and the electrolyte volume, thereby operating the system in a forced convection, ideal "near-zero-gap/low-gap" configuration. This simplification aims to isolate the pure effects of temperature, concentration and cell geometry (d and ε) by decoupling the complex two-phase flow dynamics from the electrochemical solution. Consequently, the ohmic losses predicted by the model represent the lower limit (most optimistic case) achievable by the technology, particularly at high current densities (e.g., >10 kA/m^2) where gas bubbles covering the electrode surface increase resistance.

Within the scope of this study, modelling is limited to steady-state operating conditions. Dynamic (transient) operating scenarios that are important in electrolyser applications dependent on renewable sources (such as load fluctuations, start-up/shutdown cycles and short-term current changes) are excluded from the scope of this study. The fundamental reason for this is that the aim of the study is not to examine time-dependent control and transient regime behaviour, but rather to reveal how physically resolved performance outputs at the cell level are reflected in technical–economic analyses. Although the presented two-stage framework is, in principle, extendable to transient models, such an extension requires additional differential equations, time-dependent material properties and dynamic cost definitions, and is therefore considered a topic for future work.

In order to systematically investigate the factors affecting the electrolysis performance, five operating variables were screened separately: temperature, electrolyte concentration, electrode–separator distance, electrolyte type (KOH/NaOH) and separator porosity. The parameter ranges were 25–75 °C, 6–12 mol·L^{-1}, 2–4 mm, KOH/NaOH and 0.30–0.40, respectively. A "one-parameter-at-a-time" approach was applied, whereby only one variable was changed in each scenario, while the remaining four variables were kept constant and the relative effects were decomposed. The list of analyses, along with the varying parameters, is given Table 3.

Table 3. Parametric combinations of operating conditions and design variables used in the electrochemical performance analysis.

#	Temperature (°C)	Electrolyte Concentration (mol·L)	Electrode–Separator Distance (mm)	Separator Porosity	Electrolyte
1	25	6	2	0.3	KOH
2	25	10	2	0.3	KOH
3	25	6	4	0.3	KOH
4	25	10	4	0.3	KOH
5	25	6	4	0.4	KOH
6	50	6	2	0.3	KOH
7	50	10	2	0.3	KOH
8	50	6	4	0.3	KOH
9	50	10	4	0.3	KOH
10	75	6	2	0.3	KOH
11	75	6	4	0.3	KOH
12	25	6	2	0.4	KOH
13	75	6	2	0.4	KOH
14	50	6	2	0.4	KOH
15	25	6	2	0.3	NaOH
16	25	6	4	0.3	NaOH
17	50	6	2	0.3	NaOH
18	50	6	4	0.3	NaOH
19	75	6	2	0.3	NaOH
20	25	6	4	0.4	NaOH

Table 3 summarizes 20 scenarios designed to study the effect of a specific parameter in the electrolysis process. In each case, I–U curves were generated in the range 1.23–1.98 V and the corresponding average current densities were calculated. A single parameter was systematically varied while other variables were held constant, thus isolating the marginal effect of each factor on cell voltage, efficiency and overall performance. This setup quantitatively and comparatively reveals the contribution of the variables to the electrolysis behaviour. In the parametric analysis, temperature (25–75 °C), concentration (6–12 mol·L^{-1}), electrode–separator gap (2–4 mm), separator porosity (0.30–0.40) and electrolyte type (KOH and NaOH) were systematically varied. The temperature increase shifted the polarization curves downward, reducing the required cell voltage and increasing the current density. The concentration change quantified the sensitivity of conductivity and efficiency. The gap was identified as the main lever determining ohmic losses and voltage requirements, while porosity determined ion transport and overall performance. The KOH–NaOH comparison demonstrated that electrolyte selection creates significant differences in the voltage–current relationship depending on the conditions. This design matrix provides a solid foundation for identifying the most favourable operating conditions for performance improvement by clarifying the effects of variables.

The reliability of the model was verified by comparison with experimental polarization curves reported in the literature, e.g., Refs. [56,59]. The fit parameters (r, t, n, z, etc.) were calibrated against these datasets, and consistency with COMSOL outputs for each scenario was achieved within a maximum deviation of ±3%. The parameter values were optimized to stay within the ranges specified in Table 2. "$i_{0,a}$" and "$i_{0,c}$" are the "reference exchange current density" parameters used in the COMSOL Water Electrolyser interface. They have been selected to be consistent with the apparent/effective value ranges reported in the literature [60] and also represent the effective active area/roughness effects of the electrode.

Cost optimization is essential to link performance findings with economic viability. In this study, AWE costs are derived from the year-end 2024 market data compiled in Table 4, covering the bulk–module–system components for different system scales. These cost inputs are compiled from international energy agency and industry databases for the reference year 2024. In particular average values from different reports, news, and summaries, as well as European-based supplier quotes and open databases, are compiled [61–65]. The data are combined using a weighted average method and normalized to nominal 2024 USD to reflect regional price differences. This diversity of sources strengthens the timeliness, transparency and generalizability of the model across scales. Using this dataset, the unit cost per active area is calculated and calibrated to a single-cell cost of 19,200 \$·m^{-2}, which includes materials, labour and project items, with the aid of EES (Engineering Equation Solver). The single-cell cost expressed per active area was obtained by converting the reported stack/module cost information into an area-normalized metric, i.e., \$·m^{-2} = (stack or cell-package cost)/(total active area). The resulting value (19,200 \$·m^{-2}) therefore represents an aggregate "cell package" cost that includes the electrochemical core components and immediate hardware required at the cell/stack level (e.g., electrodes, separator/diaphragm, current collectors, frames, sealing and assembly-related items), consistent with the cost categories used in Table 4. This area-based calibration enables a coherent link between the electrochemical model outputs (current density, voltage and efficiency) and the cost module implemented in EES.

In addition to parametric analysis, an independent study was conducted for cost optimization. Under conditions of 75 °C, 6 M KOH, separator porosity 0.80 and electrode–separator gap 2 mm, the current–voltage data obtained by sampling the cell voltage in the range of 1.8–2.5 V were continuous using an appropriate regression and applied in closed form in the EES environment, as Equation (4). The current densities derived from this relationship were interpreted on a per-unit-area basis, and the total active area required for the target power was calculated using Equation (5). The stack cost, covering only cell production, was determined based on this area-dependent relationship (6):

$$V_{cell} = -0.000000000293 \cdot I_{cell}{}^{2} + 0.0000627 \cdot I_{cell} + 1.816 \quad (4)$$

$$A_{total} = (W_{total}/V_{cell} \cdot I_{cell}) \cdot 1000 \quad (5)$$

$$Cost_{stack} = A_{total} \cdot 19{,}200 \quad (6)$$

Table 4. Cost and scaling factors for alkaline electrolysis systems at different sizes. Data sources for market prices and cost items are provided in Refs. [61–65] and all monetary values are reported in nominal 2024 USD after inflation adjustment [66] (in Appendix A).

System Size (kWh)	Stack ($)	Mod ($)	Systems ($)	Module Factor (F_m)	System Factor (F_s)
25	25,000	90,000	160,000	3.600	1.778
250	150,000	350,000	450,000	2.333	1.286

Current 25 and 250 kW market prices have been compiled from manufacturer quotes, industry reports and open databases, with larger capacities estimated by interpolation from existing unit prices. Based on this, two scale factors have been defined: the system factor F_s represents the cost share of auxiliary/integration items such as power electronics, piping, and control; the module factor F_m represents the unit cost change depending on the module scale, capturing the relatively high installation and production costs at small capacities due to limited economies of scale.

The functional relations of these scaling coefficients are defined by F_s in Equation (7) and F_m in Equation (8). The maintenance coefficient, which represents the burden of maintenance, repair labour and spare parts, is taken as F_{mn} = 1.3. It has been selected as a conservative midpoint value, falling within the typical range of 1.2–1.4 reported in the literature [67]. Capital expenditures (CapEx) are calculated using these coefficients according to Equation (9) and operating items other than energy expenditures are considered in the same framework. These scale factors are based on validated module-and-system scaling relationships in the literature [61,64]. The 25 and 250 kW references were selected as two practical boundary cases representing commercial module data; the F_s and F_m parameters were extrapolated up to the 10 MW order via log-linear trends capturing power component cost elasticities. This extrapolation follows the well-established power law scaling commonly used in process and energy system cost estimation, where the total system cost (or a given cost component) scales with capacity as $C(P) = C(P_{ref}) \cdot (P/P_{ref})^{k}$, which becomes linear in log–log space ($\log C = \log C_{ref} + k \log(P/P_{ref})$). Accordingly, the log-linear trend used here represents a standard economy-of-scale formulation. The 25 kW and 250 kW points were selected to anchor the scaling across the small commercial range, and the resulting exponent provides a consistent basis for extending the cost model to MW-scale systems [68].

While a two-point calibration inevitably introduces uncertainty in the absolute CAPEX prediction at very large scales, it preserves the comparative trends required for the integrated performance–cost assessment performed in this study. A brief sensitivity check on the scaling exponent (within ranges commonly reported for modular electrolysis systems) confirmed that the qualitative LCOH trends reported in this study remain unchanged, with electricity price remaining the dominant driver of LCOH across scales. This method is consistent with the scale–cost reduction rates ($-0.25 \leq (\partial \ln(CAPEX))/(\partial \ln(power) \leq -0.15)$)

presented in the global reports, accurately capturing a 15–25% unit CAPEX decreases at the MW scale [61,63].

$$F_s = 2.0642 \cdot {W_{total}}^{-0.063} \tag{7}$$

$$F_m = 5.7676 \cdot {W_{total}}^{-0.156} \tag{8}$$

$$CapEx = Cost_{stack} \cdot F_s \cdot F_m \cdot F_{mn} \tag{9}$$

The system is assumed to have an operational lifetime of 20 years and a capacity factor of 85%, taking into account maintenance, repair and operational outages. For electricity cost, LCOE = 0.05 and 0.10 $\$\cdot kWh^{-1}$ scenarios are adopted to represent regional differences and variability due to generation source (renewable/fossil). Under these assumptions, Operational Expenditures (OpEx) are calculated according to Equation (10):

$$OpEx = LCOE \cdot W_{total} \cdot Life \cdot Capacity \cdot Annual\ Hours \tag{10}$$

In this study, where the total cost (CapEx + OpEx) is taken as a basis, LCOH was obtained in the following order. First, the hydrogen production efficiency was determined by Equation (11), where the constant 1.46 represents the theoretical upper limit derived from LHV = 33.3 $kWh\cdot kg^{-1}$ and the thermoneutral voltage of 1.23 V. The hourly production is then linked to power and efficiency by Equation (12), which includes the constant HHV = 39.4 $kWh\cdot kg^{-1}$, and the cumulative lifetime production is calculated from Equation (13). In the final stage, LCOH was found as the ratio of total cost to lifetime production according to Equation (14).

$$\eta_{H2} = 1.46/V_{cell} \tag{11}$$

$$H_{2,perhour} = (W_{total} \cdot \eta_{H2})/39.4 \tag{12}$$

$$H_{2,total} = H_{2,perhour} \cdot Life \cdot Capacity \cdot Annual\ Hours \tag{13}$$

$$LCOH = (CapEx + OpEx)/H_{2,total} \tag{14}$$

The contributions of CapEx and OpEx to the total cost were analyzed separately using Equations (15) and (16). Furthermore, the unit hydrogen production costs per kg contributions of CapEx and OpEx were clarified using Equation (17) and Equation (18), respectively.

$$CapEx_{cont} = CapEx/Total\ cost \tag{15}$$

$$OpEx_{cont} = OpEx/Total\ cost \tag{16}$$

$$CapEx_{perH2} = CapEx/H_{2,total} \tag{17}$$

$$OpEx_{perH2} = OpEx/H_{2,total} \tag{18}$$

This systematic approach provides a detailed framework for cost optimization in alkaline water electrolyzers and ensures that all relevant factors are comprehensively evaluated. The general flow of the steps followed in the modelling process is summarized in Figure 2.

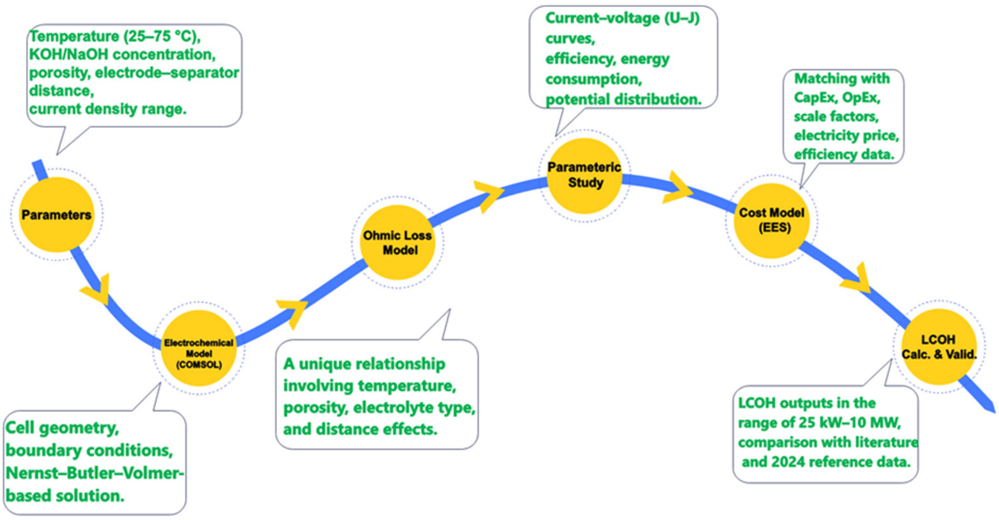

Figure 2. Methodology flowchart. The modelling process includes defining input parameters, COMSOL-based electrochemical solution, applying the extended ohmic loss model, performing parametric analyses, integrating the cost model (EES) and LCOH calculation and verification steps.

3. Results and Discussion

In this study, the physical behaviour of the electrolyzer was first evaluated using polarization curves obtained with COMSOL Multiphysics, and, to demonstrate the quantitative reliability of the proposed framework, the electrochemical model was validated using experimental data reported by Rodriguez et al. [69] for an alkaline cell operating at 25 °C with 30% KOH by weight. To ensure a consistent comparison, the experimental current density values were converted from $mA{\cdot}cm^{-2}$ to $A{\cdot}m^{-2}$. As shown in Figure 3, the simulation results (based on a fundamental 2 mm electrode–separator gap) exhibit a strong correlation with experimental measurements, achieving deviation of less than 3% in the 0–2000 $A{\cdot}m^{-2}$ range. The model accurately captures the activation onset at ~1.48 V and matches the nominal operating point of ~1.88 V at 1000 $A{\cdot}m^{-2}$. The marginal voltage increase observed at higher current densities in the simulation is attributed to the additional ohmic resistance caused by the 2 mm gap compared to the physically gapless experimental setup. Furthermore, the technical–economic outputs were compared with 2024 global strategic reports; the calculated LCOH range (4.1–5.9 kg^{-1}) falls squarely within the ranges published by the IEA (3.8–6.0 kg^{-1}) [61] and the Hydrogen Council (4.5–6.5 kg^{-1}) [63], confirming the model's validity in both the physical and economic domains. The primary objective of this study is to elucidate the physical effects of temperature, electrode–separator distance, separator porosity, electrolyte concentration and electrolyte type on cell performance, and to evaluate the ultimate implications of these effects on LCOH. The in-plane potential distributions and current paths presented in Figures 4 and 5 clearly illustrate the underlying electrochemical mechanisms of the interpreted trends; they qualitatively support the relationship between ionic conduction paths, potential gradients and ohmic losses.

COMSOL-based analyses were structured around five main parameters—temperature, electrode–separator distance, separator porosity, electrolyte concentration and electrolyte type—all of which were decomposed in a "one-parameter-at-a-time" approach, holding other variables constant and thus focusing on the marginal contribution to average cell current density. The representative electrolyte potential/gradient maps and current density vector fields (Figure 4) are presented to support the physical interpretation of the findings; these visualizations qualitatively reveal the effects of parameter variations on in-field potential homogeneity, ohmic drop magnitude and ion transport efficiency, and provide a consistent framework with quantitative I-U analyses.

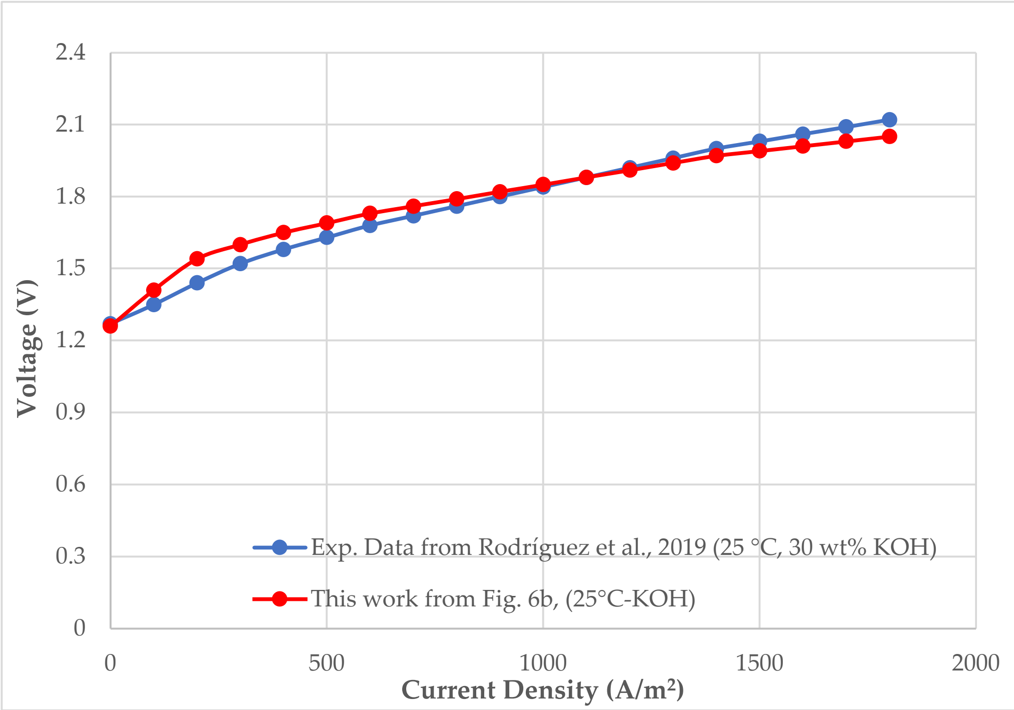

Figure 3. Validation of the electrochemical model against experimental data. The solid red line represents the simulation results of this study (6 M KOH, 25 °C and 2 mm electrode–separator gap). The blue markers represent independent experimental data reported by Rodriguez et al. [69] for an alkaline electrolysis cell (30 wt% KOH, 25 °C).

The increase in temperature enhances the ionic conductivity of the electrolyte, leading to a more homogeneous potential distribution and reducing the ohmic overpotential. This allows the polarization curves to shift downwards across the entire voltage range and enables higher current densities to be achieved at the same operating voltage (Figure 5). This physical improvement is directly reflected in the economic model as lower specific electricity consumption and, consequently, lower LCOH values. However, it should be noted that the increase in temperature brings additional requirements for the system design, such as heat management and material durability.

Increasing the separator porosity of the separator facilitates ion transport, thereby enhancing effective ionic conductivity and reducing ohmic losses. As shown in Figure 5, increasing the separator porosity from 0.30 to 0.40 provides a significant increase in current density, particularly in the low and medium temperature ranges. This finding demonstrates that the separator microstructure must be optimized not only in terms of material selection but also in relation to the target operating temperature and operating conditions.

The electrode–separator distance is one of the most critical geometric parameters defined by the model. The current density vector fields in Figure 4 clearly demonstrate that as the distance increases, the ion transport path lengthens and local potential gradients increase. This situation leads to a decrease in the average current density across all voltage ranges. The electrolyte type (KOH or NaOH) does not alter this fundamental trend; however, KOH yields higher performance due to its higher conductivity. The fact that increased ohmic losses translate to higher operating voltage makes this parameter a powerful economic design lever.

When electrolyte concentration and type are considered together, it is observed that KOH solutions operate at lower cell voltages compared to NaOH due to their higher conductivity (Figure 6). Increasing the concentration enhances conductivity up to a certain point, but this gain becomes limited at high concentrations. Furthermore, it is observed that the performance difference between KOH and NaOH decreases as the temperature rises. These results indicate that the choice of electrolyte should be considered not only on a chemical or cost basis, but also in terms of its effects on system efficiency and energy consumption.

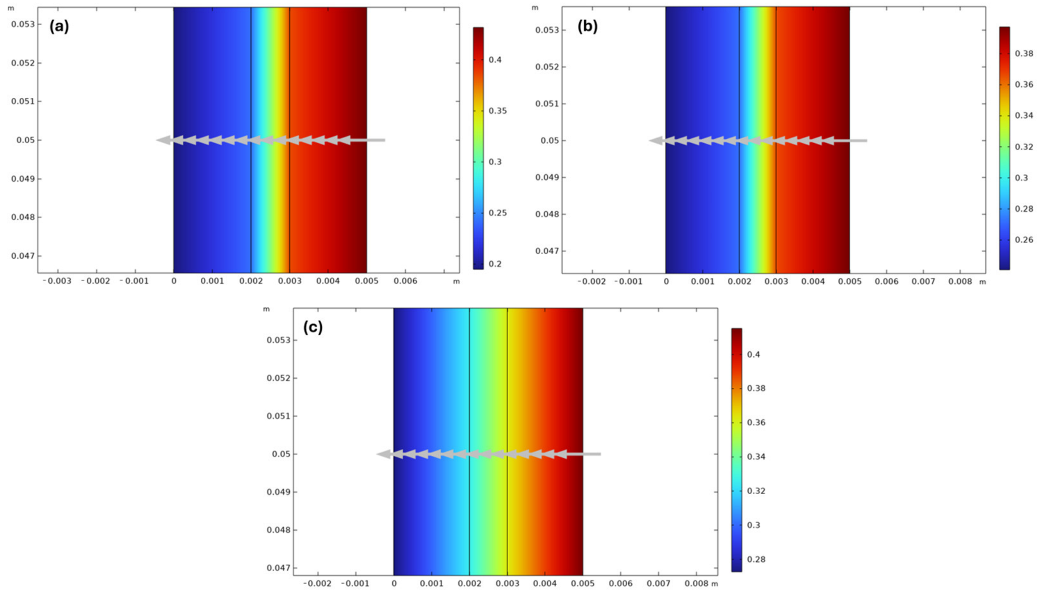

Figure 4. Analysis of the electrolyte potential and current field. (**a**) Base case (Analysis 1; U = 1.98 V): A regular potential drop across the field and accompanying current paths are observed; when the applied voltage changes, the spatial pattern is preserved, and the drop magnitude and vector intensity are scaled. (**b**) Temperature scan (Analysis 10; U = 1.98 V and T = 25–75 °C): while the shape of the potential distribution remains essentially constant, the increase in temperature raises the electrolyte conductivity; this leads to a decrease in the ohmic drop and a sharpening of the current vectors (consistent with the I–U sensitivities). (**c**) High separator porosity configuration (U = 2.03 V): increased porosity enhances the separator's effective conductivity, causing the red regions to narrow (lower potential drop) and current paths to concentrate; consequently, ohmic losses decrease and cell efficiency improves. The arrows indicate the electrolyte current density, showing the direction and relative magnitude of ion flow.

The fundamental reason for the narrowing of the performance difference between KOH and NaOH as temperature increases is the differing responses of the ionic conductivities of both electrolytes to temperature. At low temperatures, KOH solutions exhibit significantly higher conductivity compared to NaOH due to higher ion mobility and lower viscosity. However, as temperature increases, the viscosity and hydration constraints on ion transport in NaOH solutions decrease more rapidly, and the rate of the conductivity increase approaches that of KOH. The conductivity–temperature relationships reported in the literature indicate that the temperature-dependent conductivity increase for NaOH has a higher relative slope. This leads to a decrease in the effective conductivity difference between the two electrolytes at high temperatures and, consequently, a narrowing of the performance difference in the polarization curves. The trends observed in the model results are consistent with this physical conductivity behaviour.

The sensitivity trends observed in the polarization curves directly reflect changes in the electrical energy demand required for unit hydrogen production, and this effect plays a decisive role on LCOH within the proposed framework. Reducing the electrode–separator distance and increasing effective ionic conductivity (through improvements in temperature, electrolyte concentration and separator structure) lowers the cell operating voltage at a given current density; this leads to a reduction in specific energy consumption and, consequently, a measurable decrease in the LCOH value.

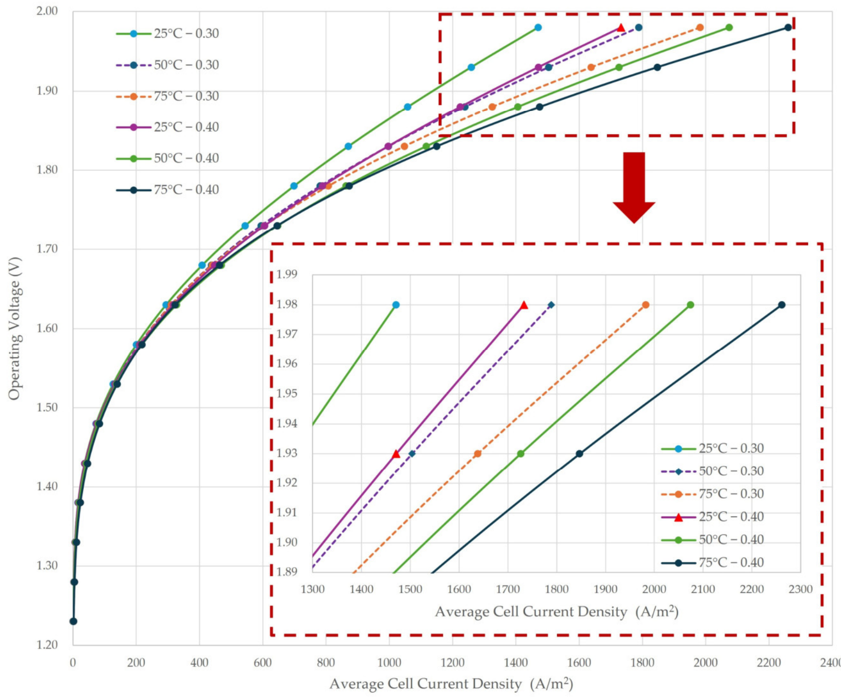

Figure 5. Effect of temperature and separator porosity. The relationship between operating voltage (V) and average cell current density (I) is shown for three temperatures (25, 50 and 75 °C) and two porosities (ε = 0.30; 0.40) (KOH 6 M; electrode–separator distance 2 mm). As temperature and porosity increase, the curves shift downward; lower U is required for the same J (e.g., at U = 1.98 V, I for ε = 0.30 is 25 → 50 → 75 °C; ~1733 → 2074 → 2261 $A \cdot m^{-2}$ for ε = 0.40). The enlarged panel highlights that small voltage increases in the 1.88–1.98 V band lead to disproportionate increases in I. The trends are consistent with the decrease in ohmic drops resulting from increased ionic/effective conductivity.

When evaluating model results, it is important to note that neglecting the bubbling effects imposes a limitation on the accuracy of ohmic overvoltage predictions, particularly at high current densities. In real-world applications, gas bubbles reduce the effective conductivity of the electrolyte (according to the Bruggeman approach) and this leads to higher cell voltages than those predicted by single-phase models. In our study, a "best-case" scenario was simulated, assuming perfect bubble management and gas venting. Therefore, the LCOH values presented, particularly for high current densities such as 20 kA/m^2, should be interpreted as the theoretical economic potential that this technology could achieve under perfect mass transfer conditions. Operational conditions involving significant bubble accumulation will result in marginally higher voltages and, consequently, slightly higher LCOH values compared to the baseline projections presented in this study.

The one-dimensional voltage–current relationships obtained from COMSOL were combined with a cost module developed in the EES environment to optimize the levelized cost of hydrogen (LCOH) for alkaline electrolyzers. The approach is applied to 25, 100, 1000, 5000 and 10,000 kW systems by matching the technical outputs derived from current density, voltage and efficiency with capital and operating costs and incorporating scale effects. The analyses were conducted for two electricity cost scenarios (0.05 $\$ \cdot kWh^{-1}$ and 0.10 $\$ \cdot kWh^{-1}$) and two current density levels (10,000 and 20,000 $A \cdot m^{-2}$); in each scenario, CapEx and OpEx were decomposed, lifetime hydrogen production was calculated and LCOH was derived based on this (20 analyses in total).

When considering the sensitivity analysis presented, while adopting a "single-parameter-at-a-time" approach to isolate the specific effect of each design variable, it is important to acknowledge the complex physical interactions governing the system. Most notably, the interaction between the operating temperature (T) and electrolyte concentration

(C) produces a non-linear synergistic effect on ionic transport. For example, increasing the concentration generally improves ionic conductivity, but it also increases dynamic viscosity. This can inhibit mass transport, but this inhibition is significantly reduced at high temperatures due to the thermal thinning effect. Although the graphs presented in this study visualize the parameters individually, the underlying electrochemical model (as defined in the EES subfields) naturally captures these interdependencies through temperature- and concentration-dependent property functions. Consequently, the reported performance trends reflect these physical synergies and enable the effect of altering one parameter to be calculated within the consistent physical context of the others.

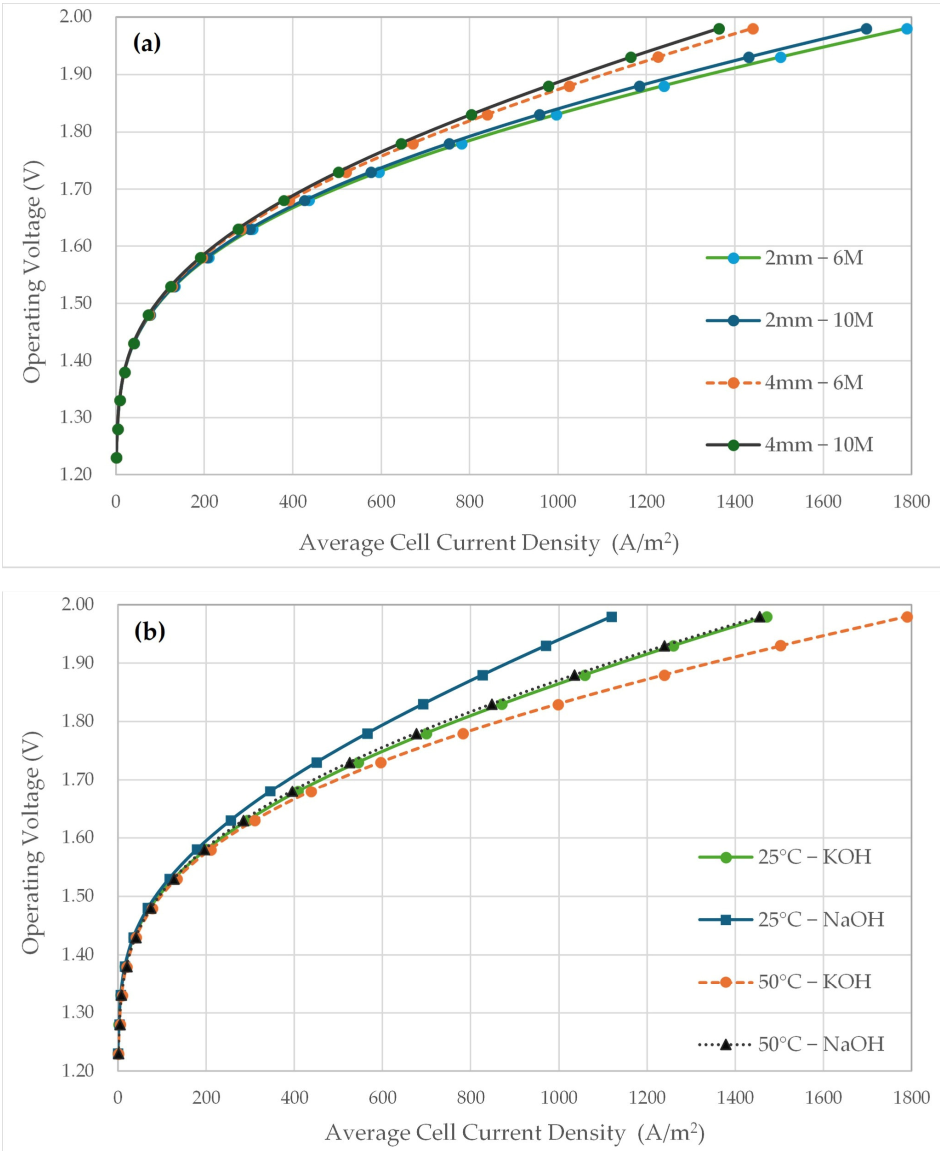

Figure 6. Effects of geometry–concentration (**a**) and electrolyte–temperature (**b**): (**a**) The I–V relationship is shown for KOH at two cell gaps (2 and 4 mm) and two concentrations (6 and 10 M). Increasing the cell gap to 4 mm shifts the curves significantly upward, requiring higher V for the same I; increasing the concentration to 10 M produces a similar but weaker upward shift. (**b**) Comparison of KOH and NaOH at 25 °C and 50 °C (6 M; electrode–separator distance 2 mm; and porosity 0.30). At 25 °C, the NaOH curve is systematically higher than that of KOH; at 50 °C, both curves shift downward and the difference between them narrows significantly. The findings indicate that a narrow cell gap–medium concentration combination should be preferred to limit ohmic losses, and that electrolyte–temperature co-optimization is desirable for performance.

The LCOH results obtained by reflecting these physical assessments in the techno-economic model are summarized in Tables 4 and 5. The dominant effect of electricity prices on total costs is confirmed in all scenarios. While every improvement in performance reduces LCOH, energy prices emerge as the most decisive component at both small and large scales. Although unit CAPEX decreases as scale increases, the share of electricity consumption in the total is high, so the overall trend of LCOH is shaped by the unit cost of electricity. The LCOH values for an electricity unit price of 0.05 $\$\cdot kWh^{-1}$ and 0.10 $\$\cdot kWh^{-1}$ are compared for different electrolyzer scales ranging from 25 kW to 10 MW. The curves show that CAPEX decreases as the scale increases, but the electricity cost remains the main determinant of the total cost (Figure 7).

Table 5. System-scale techno-economic and performance results of alkaline water electrolysis under different system sizes and current densities, including cell area, operating voltage, scaling factors (F_m, F_s), system efficiency, and total hydrogen production.

#	System Size (kWh)	Current Density ($A\cdot m^{-2}$)	LCOE ($\$\cdot kWh^{-1}$)	Total Cell Area (m^2)	Voltage (V)	F_m	F_s	System Eff.	Produced Total H_2 (Ton)
1	25	10,000	0.05	1.036	2.414	3.49	1.68	0.605	57.2
2	25	20,000	0.05	0.4233	2.953	3.49	1.68	0.494	46.7
3	25	10,000	0.1	1.036	2.414	3.49	1.68	0.605	57.2
4	25	20,000	0.1	0.4233	2.953	3.49	1.68	0.494	46.7
5	100	10,000	0.05	4.143	2.414	2.81	1.54	0.605	228.6
6	100	20,000	0.05	1.693	2.953	2.81	1.54	0.494	186.9
7	100	10,000	0.1	4.143	2.414	2.81	1.54	0.605	228.6
8	100	20,000	0.1	1.693	2.953	2.81	1.54	0.494	186.9
9	1000	10,000	0.05	41.43	2.414	1.96	1.34	0.605	1869
10	1000	20,000	0.05	16.93	2.953	1.96	1.34	0.494	1869
11	1000	10,000	0.1	41.43	2.414	1.96	1.34	0.605	2286
12	1000	20,000	0.1	16.93	2.953	1.96	1.34	0.494	1869
13	5000	10,000	0.05	207.2	2.414	1.53	1.21	0.605	11,430
14	5000	20,000	0.05	84.67	2.953	1.53	1.21	0.494	9344
15	5000	10,000	0.1	207.2	2.414	1.53	1.21	0.605	11,430
16	5000	20,000	0.1	84.67	2.953	1.53	1.21	0.494	9344
17	10,000	10,000	0.05	414.3	2.414	1.37	1.15	0.605	22,860
18	10,000	20,000	0.05	169.3	2.953	1.37	1.15	0.494	18,690
19	10,000	10,000	0.1	414.3	2.414	1.37	1.15	0.605	22,860
20	10,000	20,000	0.1	169.3	2.953	1.37	1.15	0.494	18,690

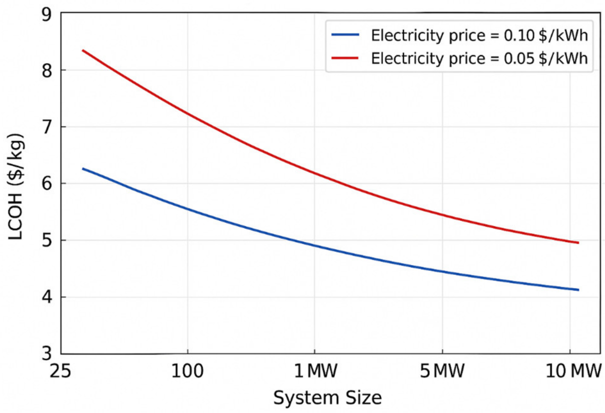

Figure 7. LCOH variation with system scale and electricity price.

The results presented in Figure 4 show that the electrolyte conductivity increases with rising temperature, and consequently, the ohmic overpotential decreases. When evaluating the economic implications of this trend, it is observed that a 10 °C increase in operating temperature at a representative operating point reduces the cell operating voltage by several tens of millivolts; this voltage reduction corresponds to an improvement in the specific electricity consumption of approximately one per cent. This improvement is reflected in the technical–economic model through direct electricity consumption in LCOH calculations and provides a measurable reduction in the LCOH value depending on the system scale (Figure 7).

Similarly, when the electrochemical and economic effects of the increase in separator porosity are evaluated together, it is seen that increasing the separator porosity by 0.05 increases the effective ionic conductivity and reduces ohmic losses. This improvement observed in the polarization curves allows for operation at a lower cell voltage at a given current density; as a result, the specific energy consumption decreases and a direct positive effect is observed on the LCOH. The model results show that a separator porosity increase at this level corresponds to a percentage decrease in the LCOH value when the other parameters are held constant.

The model curves match the trends and orders of magnitude of the near-zero-gap/low-gap AWE data in the literature; differences are concentrated in the activation region at low currents and in the ohmic region at high currents [69,70].

LCOH calculations were performed using two representative current densities (10 $kA \cdot m^{-2}$ and 20 $kA \cdot m^{-2}$) to demonstrate system behaviour under different operating conditions. Each scenario represents a specific current density–efficiency–voltage combination; therefore, LCOH is not a precise value for a single operating point, but rather a metric that reveals the relative position of cost–efficiency trade-offs within a wide operating range. This approach has been generalized to cover the performance ranges of actual electrolysers under variable load conditions.

The LCOH calculated for an electricity cost of 0.05–0.10 $\$ \cdot kWh^{-1}$ and a scale range of 25 kW–10 MW falls within the public bands reported in 2024 by the International Energy Agency (IEA) and Hydrogen Council; $\geq$10 $kA \cdot m^{-2}$ scenarios are considered as upper-bound sensitivities rather than as typical operation scenarios [61,63].

When the electricity cost is 0.05 $\$ \cdot kWh^{-1}$, as the scale increases, the LCOH declines from approximately 5.9 $\$ \cdot kg^{-1}$ for 25 kW to 4.4 $\$ \cdot kg^{-1}$ for 1 MW and slightly below 4.0 $\$ \cdot kg^{-1}$ for 10 MW (Table 6). When the electricity cost is 0.10 $\$ \cdot kWh^{-1}$, the LCOH rises to approximately 9.2, 7.7 and 7.2 $\$ \cdot kg^{-1}$ at the same scales, meaning that a doubling of the electricity price significantly increases the cost across all capacities. Increasing the current density from 10,000 $A \cdot m^{-2}$ to 20,000 $A \cdot m^{-2}$ reduces the LCOH by approximately 5–10% in small systems, while efficiency losses become dominant at the MW scale, increasing the costs by approximately 3–9%. This effect is more pronounced at high electricity costs; for example, at 10 MW and 0.10 $\$ \cdot kWh^{-1}$, a high current density yields an LCOH of approximately 8.33 $\$ \cdot kg^{-1}$, which is significantly higher than the low-cost baseline scenario. These results show that the primary determinant of total cost is the electricity price, and that an increase in current density only provides a net economic advantage under low-cost electricity conditions. The relevant parametric sensitivity findings are summarized in Table 7.

Table 8 summarizes the impacts of the two scenarios on the total cost and LCOH for capacities between 25 kW and 10 MW. Increasing the current density from 10,000 to 20,000 $A \cdot m^{-2}$ significantly reduces the total cost, especially at small scales. However, while LCOH improves in small systems, it may show limited increases in large systems due to efficiency loss. Increasing the cost of electricity from 0.05 to 0.10 $\$ \cdot kWh^{-1}$ significantly increased both total cost and LCOH at all scales, and the effects were larger in relative and absolute terms for large systems with higher energy consumption. The findings suggest that the primary determinant of cost is the electricity price, while a current density increase requires a scale-dependent trade-off of benefits and efficiency.

Table 6. Breakdown of capital (CapEx) and operating (OpEx) expenditures and their respective contributions to the levelized cost of hydrogen (LCOH) and total system cost for alkaline water electrolysis systems at different system sizes and current densities.

#	Sys. Size (kWh)	Current Density ($A \cdot m^{-2}$)	LCOE ($\$ \cdot kWh^{-1}$)	CapEx ($M)	OpEx ($M)	LCOH ($\$ \cdot kg^{-1}$)	CapEx ($/kg)	OpEx ($/kg)	Total Cost ($M)
1	25	10,000	0.05	0.152	0.186	5.918	2.66	3.26	0.338
2	25	20,000	0.05	0.062	0.186	5.315	1.33	3.98	0.248
3	25	10,000	0.1	0.152	0.372	9.175	2.66	6.51	0.524
4	25	20,000	0.1	0.062	0.372	9.299	1.33	7.97	0.434
5	100	10,000	0.05	0.449	0.745	5.221	1.96	3.26	1.194
6	100	20,000	0.05	0.184	0.745	4.966	0.98	3.98	0.928
7	100	10,000	0.1	0.449	1.489	8.478	1.96	6.51	1.938
8	100	20,000	0.1	0.184	1.489	8.951	0.98	7.97	1.673
9	1000	10,000	0.05	2.712	7.446	4.443	1.19	3.26	10.158
10	1000	20,000	0.05	1.108	7.446	4.577	0.59	3.98	8.554
11	1000	10,000	0.1	2.712	14.890	7.700	1.19	6.51	17.602
12	1000	20,000	0.1	1.108	14.890	8.562	0.59	7.97	15.998
13	5000	10,000	0.05	9.532	37.230	4.091	0.83	3.26	46.762
14	5000	20,000	0.05	3.896	37.230	4.401	0.42	3.98	41.126
15	5000	10,000	0.1	9.532	74.460	7.348	0.83	6.51	83.992
16	5000	20,000	0.1	3.896	74.460	8.385	0.42	7.97	78.356
17	10,000	10,000	0.05	16.380	74.460	3.973	0.72	3.26	90.840
18	10,000	20,000	0.05	6.695	74.460	4.342	0.36	3.98	81.155
19	10,000	10,000	0.1	16.380	148.900	7.230	0.72	6.51	165.280
20	10,000	20,000	0.1	6.695	148.900	8.327	0.36	7.97	155.595

Table 7. Sensitivity of LCOH to changes in capital (CapEx) and operating (OpEx) expenditures for alkaline water electrolysis systems at different system scales, showing absolute and relative cost variations and their impact on LCOH.

System (kW)	CAPEX				OPEX			
	Change ($M)	Change (%)	LCOH Change ($\$ \cdot kg^{-1}$)	LCOH % Change	Change ($M)	Change (%)	LCOH Change ($\$ \cdot kg^{-1}$)	LCOH % Change
25	−0.09	−59.21	−0.603	−10.1	0.186	100	3.257	55.0
100	−0.265	−59.02	−0.255	−4.8	0.745	100	3.257	62.3
1000	−1.604	−59.14	0.134	3.0	7.446	100	3.257	73.3
5000	−5.636	−59.13	0.31	7.5	37.23	100	3.257	79.6
10,000	−9.685	−59.13	0.369	9.2	74.46	100	3.257	81.9

Although increased current density provides a certain advantage in small-scale systems, efficiency losses become more dominant at the MW scale. Therefore, the optimal operating range is found to be 8–12 $kA \cdot m^{-2}$. The quantitative results presented in Table 8 clearly reveal the economic mechanism behind this optimal operating range. Although the system operates with higher electrochemical efficiency at low current densities, the increase in the required active area increases stack and system costs, and capital expenditure (CapEx) becomes dominant over LCOH. Conversely, increasing the current density reduces the active area requirement, thereby lowering CapEx; however, this time, the specific electricity consumption rises due to the increased cell operating voltage and decreased system efficiency, and operating expenses (OpEx), particularly through electricity costs, begin to become decisive for the LCOH.

https://doi.org/10.3390/en19030835

Table 8. Total system cost and LCOH under doubled current density and electricity price scenarios for alkaline water electrolysis systems at different system sizes.

System (kW)		25	100	1000	5000	10,000
Doubled Current Density	Total Cost ($M, 10 kA·m^{-2}, LCOE = 0.05)	0.338	1.194	10.158	46.762	90.84
	Total Cost ($M, 20 kA·m^{-2}, LCOE = 0.05)	0.248	0.928	8.554	41.126	81.155
	Change in Total Cost ($M)	−0.09	−0.266	−1.604	−5.636	−9.685
	Percentage Change (%)	−26.63	−22.28	−15.79	−12.05	−10.66
	LCOH ($·kg^{-1}, 10 kA·m^{-2})	5.918	5.221	4.443	4.091	3.973
	LCOH ($·kg^{-1}, 20 kA·m^{-2})	5.315	4.966	4.577	4.401	4.342
Doubled LCOE	Total Cost ($M, LCOE = 0.05)	0.338	1.194	10.158	46.762	90.84
	Total Cost ($M, LCOE = 0.1)	0.524	1.938	17.602	83.992	165.28
	Change in Total Cost ($M)	0.186	0.744	7.444	37.23	74.44
	Percentage Change (%)	55.03	62.31	73.28	79.62	81.95
	LCOH ($·kg^{-1}, LCOE = 0.05)	5.918	5.221	4.443	4.091	3.973
	LCOH ($·kg^{-1}, LCOE = 0.1)	9.175	8.478	7.7	7.348	7.23

When these opposing trends are considered together, it is seen that increasing the current density in small-scale systems provides a net improvement in the LCOH, whereas efficiency losses become dominant at the MW scale and can increase the LCOH (see Table 8). Therefore, the range of approximately 8–12 kA·m^{-2} represents the optimal operating window where the balance between reduced capital costs and energy-related operating costs is achieved, and LCOH is minimized.

Overall, the findings show that increasing temperature, separator porosity and narrowing the gap improves performance, resulting in lower unit energy consumption and lower LCOH. The relationship between physical design decisions and economic outputs has been consistently demonstrated within the scope of the study, with energy price emerging as the determining factor in total cost across all scenarios. In general, the effect of physico-chemical parameters on cell tension is directly reflected in the economic outputs, with key variables such as temperature, separator porosity and gap shaping both performance and energy consumption. Thus, the results provide a consistent and clear link between physical trends and economic analysis.

Industrial alkaline electrolyzers typically operate in the range of 3–6 kA·m^{-2}, but the selected values of 10 kA·m^{-2} and 20 kA·m^{-2} were used as an extended parameter range to investigate the efficiency–cost limits of high-current regimes. These values are consistent with the high-current prototypes reported at the laboratory scale [71,72] and represent the maximum achievable ranges under advanced materials and fine separator configurations. Therefore, the aim is not to identify the absolute operating point, but to demonstrate the boundary conditions of the energy efficiency–economy interaction.

Figures 8 and 9 summarize the model's performance–cost relationship. In particular, the cost distribution shown in Figure 8d–f clearly demonstrates the dominant role of electricity prices in total costs. The trends in Figure 9 also support this result: as scale increases, capital costs decrease relatively, while operating costs (especially electricity costs) remain decisive in all scenarios. Therefore, the colour transitions and curve trends in the graphs directly correspond to the result emphasized in the text, namely that "electricity price is the primary determinant". From this perspective, subsections (a–c) in Figure 8 represent performance changes, while subsections (d–f) represent cost composition effects.

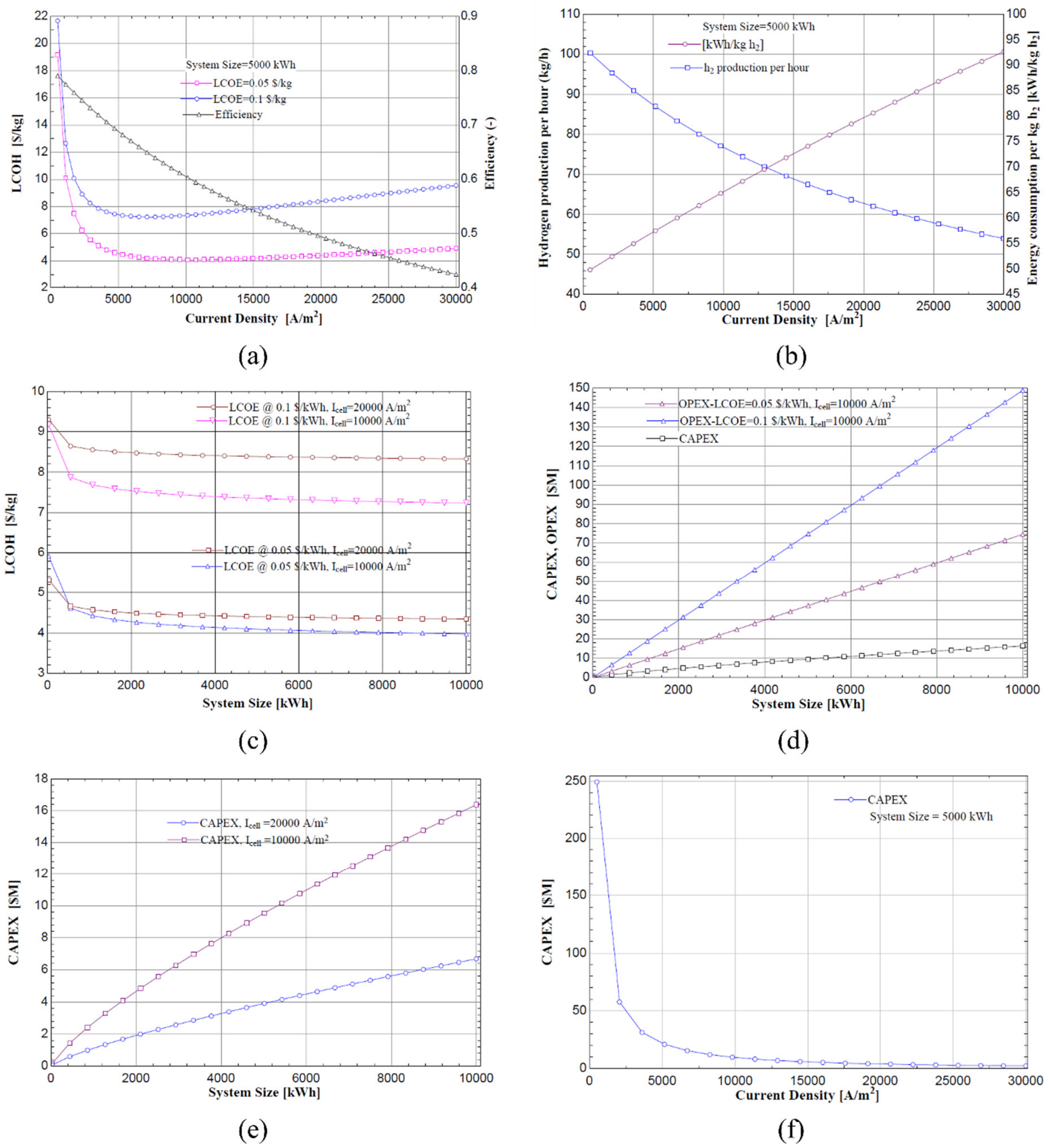

Figure 8. Parametric cost–performance diagrams (**a**–**f**). (**a**) As current density increases, cost initially decreases but is limited by efficiency loss at high values; the most favourable band is ~8–12 kA/m^2. (**b**) At 5 MWh, production rate increases and saturates, while unit energy consumption continuously rises. (**c**) Economies of scale reduce cost; the decrease weakens after 2–4 MWh, and low electricity cost is dominant at all scales. (**d**–**f**) Operating expenses, particularly at high electricity prices, are the dominant component of total costs; low current density requires larger areas and higher capital expenditure, and increasing current density at 5 MWh rapidly reduces capital expenditure, with gains improving beyond ~10 kA/m^2.

The breakdown of cost components are presented in Figure 8d–f. Figure 8d shows that although capital expenditure increases predictably with size at a constant current density, it remains secondary in the total; operating expenditure becomes the main determinant of total cost, particularly when the unit cost of electricity rises. Figure 8e reveals that when current density decreases, capital expenditure rises significantly due to the need for a larger active area for the same power and scales linearly with size. Figure 8f shows that increasing current density from very low values at a scale of 5 MWh rapidly reduces capital expenditure, that this saving reaches saturation above approximately 10 kA/m^2 and that further increases can increase operating costs due to efficiency losses. Taken together, the findings reveal that cost efficiency is maximized through low electricity costs, medium-to-high current densities remaining within the saturation band and sizing that leverages economies of scale. These results indicate that, rather than maximizing a single parameter in alkaline electrolyser design, it is necessary to select a current density sensitive to electricity prices and to prefer operating ranges that remain within the saturation band. Particularly in regions with high electricity costs, shifting the current density beyond the saturation point can lead to economically unfavourable outcomes.

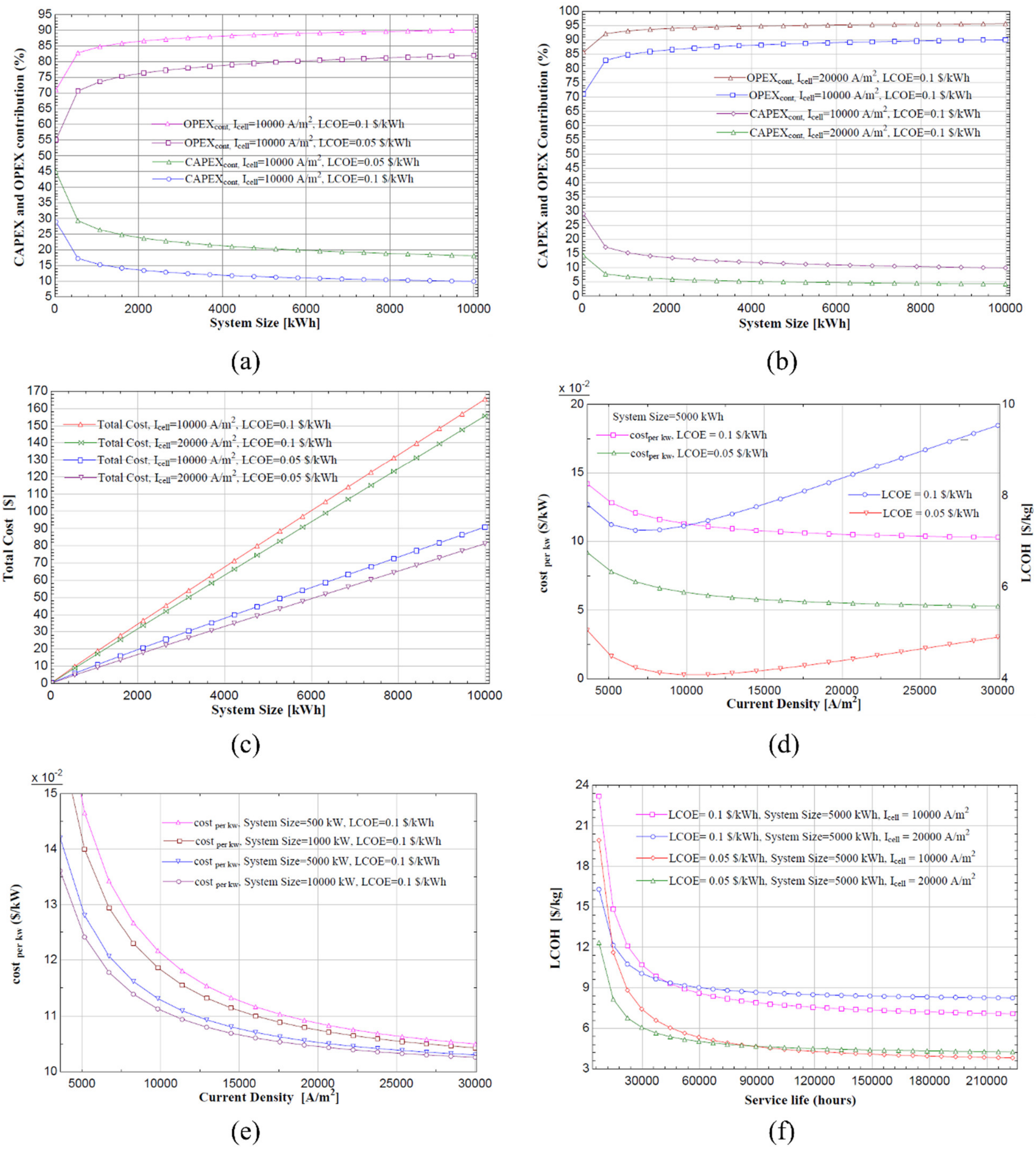

Figure 9. (**a**) Total cost vs. system size; CapEx/OpEx percentage contributions; and two electricity cost scenarios (LCOE = 0.05 and 0.10 $\$\cdot kWh^{-1}$). (**b**) CapEx/OpEx percentage contributions vs. system size; two current densities (10 and 20 $kA\cdot m^{-2}$) and two LCOEs. (**c**) Total cost vs. system size; comparison of two current densities and two LCOEs. (**d**) Cost per unit of energy and LCOH versus current density; two LCOEs. (**e**) Cost per unit of energy versus current density; different system sizes (0.5–10 MW) and fixed LCOE = 0.10 $\$\cdot kWh^{-1}$. (**f**) LCOH versus service life; fixed 5 MW system, two current densities and two LCOEs.

Figure 9 illustrates the fundamental determinants of cost composition and levelled hydrogen cost in the context of scale, current density and electricity unit cost. Figure 9a shows the percentage contribution of capital and operating expenses to total cost under different electricity cost scenarios at a constant current density. Accordingly, operating costs dominate at all scales, approaching 90 percent even at large scales with high electricity costs; they remain dominant even with low electricity costs, while capital costs stabilize in the double-digit range as the scale increases. Figure 9b highlights that increasing the current density reduces the required active area and lowers capital costs while slightly increasing operating costs due to efficiency losses; when electricity costs are low, the distribution is balanced, and when high, operating costs are decisive across all scales. Figure 9c shows that total cost increases approximately linearly with scale. The cost level depends primarily on electricity cost and secondarily on capital requirements via current density. Together, these three factors indicate that economic optimization requires reducing electricity cost and selecting current density while balancing capital and efficiency. In this context, the trends presented in Figure 9 indicate that the economic optimization of alkaline electrolysers is primarily determined by local electricity unit costs; current density and system scale are secondary design variables that must be adjusted under this fundamental constraint. Therefore, in applications with high electricity costs, aggressive increases in current density may increase operating costs rather than providing economic benefits; conversely, in low electricity cost scenarios, designs utilizing medium–high current densities and economies of scale offer more rational solutions.

Figure 9d illustrates the performance–cost perspective in terms of cost per unit of energy and levelled hydrogen cost. Under low electricity costs, the cost per unit of energy decreases rapidly as the current density increases and stabilizes in a medium–high range. At high electricity costs, the curve is higher across the entire range and rises again in the high current region. This demonstrates that the levelled cost trend is consistent with this behaviour. Figure 9e compares different scales at a fixed high electricity cost and shows that economies of scale drive down the unit energy cost across all power levels as current density increases, with gains saturating above 10–15 $\mathrm{kA \cdot m^{-2}}$. Figure 9f illustrates the service life effect at a fixed scale of 5 MW. Costs decline significantly over the first twenty years due to capital amortization, after which gains weaken. It can be stated that sustainable costs in the range of 4–5 $\$ \cdot \mathrm{kg^{-1}}$ are possible under low electricity costs and appropriately selected current densities, while a level of 9–10 $\$ \cdot \mathrm{kg^{-1}}$ is maintained under high electricity costs. Electricity price is positioned as the primary lever on cost, while current density and scale are positioned as strategic adjustment variables through the capital–efficiency. These results demonstrate that aggressively increasing current density in the design of alkaline electrolysers is not economically rational under conditions where the unit cost of electricity cannot be controlled. Conversely, in applications with low electricity costs, medium-to-high current densities within the saturation band and appropriate scale selection enable more sustainable LCOH values by balancing capital and efficiency.

The model outputs were also compared with the near-zero-gap/low-gap alkaline electrolyzer polarization curves published in the literature (Ref. [69]) and it was found that the curves showed the same trends in both the low current region and the ohmic region. Similarly, the LCOH ranges obtained in this study (4–10 $\$ \cdot \mathrm{kg^{-1}}$) are consistent with the public values reported by the International Energy Agency (IEA) and Hydrogen Council [61,63]. Two separate validations, physical and economic, show that the model reliably captures both U–J behaviour and cost estimates.

In addition, a simple sensitivity assessment was performed to summarize the relative impact of the parameters on LCOH. When parameters such as temperature, separator porosity and electrode–separator distance were individually varied by 10%, LCOH was found to decrease by approximately 8–12%, decrease by 4–7% and increase by 6–10%, respectively. In contrast, the electrolyte concentration and electrolyte type showed a more limited effect (typically 2–4%) at the same rate of variation. These results suggest that the parameters to which the model is most sensitive are temperature, separator porosity and geometric distance, with electricity cost being the dominant determinant, consistent with trends in economic outputs.

Also in this study, the degradation of the electrolyser's performance over time has not been dynamically modelled. The electrochemical performance has been assumed to be constant, representing the steady-state behaviour of the cell under nominal operating conditions. Consequently, effects such as electrode ageing, loss of catalytic activity or long-term cell voltage increase are not directly reflected in the LCOH calculations. Consequently, the cost results presented represent an optimistic lower bound based on the average or initial performance over a specific service life. The integration of long-term performance loss and the associated increase in energy consumption into the model constitutes an important focus for future studies.

4. Conclusions

This study introduces a unified framework for AWE system performance and economy by combining COMSOL-based electrochemical modelling with cost optimization using the EES module. Parameters such as temperature, electrode–separator distance, separator porosity, electrolyte concentration and electrolyte type were systematically varied; the resulting current–voltage responses were matched with capital and operational costs and linked to the LCOH. The findings indicated that temperature and separator porosity were the most influential factors on performance, with a narrow cell gap significantly reducing ohmic losses, while excessive electrolyte concentration weakened conductivity due to viscosity and saturation effects. KOH offered a more favourable electrochemical response than NaOH, although the difference diminished as the temperature increased. Economically, the key factor was the unit cost of electricity; under low LCOE conditions, and accordingly, the LCOH dropped to 4–5 $\$\cdot kg^{-1}$ at the MW scale, whereas under high LCOE conditions, it remained 7–10 $\$\cdot kg^{-1}$, which is aligned with current technological–economic analyses reporting the LCOH at the MW scale. Increasing current density reduced the active area and CapEx but decreased the efficiency, positioning the optimum in the mid-to-high range; economies of scale lowered the LCOH, though gains beyond a certain capacity were limited. The results highlighted that the simultaneous optimization of the temperature–porosity–geometry triad and local electricity prices is essential in AWE design.

- Electricity cost-focused optimization is decisive, with the LCOE being the dominant variable over the LCOH in determining the cost base at all scales.
- The use of high-porosity and low-curvature separators at elevated temperatures reduces ohmic losses and increases efficiency, and that the cell gap should be kept as narrow as possible.
- The preference for the medium concentration band and the finding that KOH requires lower voltage than NaOH, particularly at low-to-medium temperatures, has been confirmed.
- Increasing current density reduces the active area and capital expenditure but causes efficiency losses; therefore, the optimum window is formed at medium to high current densities in an electricity cost-sensitive manner.
- Economies of scale reduce the LCOH, but the rate of decrease slows significantly beyond a specific size and while costs decrease rapidly during the first twenty years of service life, the rate of decline slows markedly in the subsequent period.

This study provides a robust framework for evaluating alkaline water electrolysers, offering important information for system selection and optimization during the project development phase. By combining advanced electrochemical modelling with economic analysis, it establishes a roadmap for designing systems that achieve the lowest possible LCOH under realistic market conditions. In this respect, the study departs from the system-level and empirical technical–economic approaches prevalent in the literature, offering a validated and scalable decision support framework that directly establishes a causal relationship between intracellular physical processes and LCOH.

Overall, the findings show that it is critical to optimize the temperature–geometry–material triad together in AWE design and that the electricity price in the region where the project will be implemented is decisive on the final cost. This suggests that system selection should focus not only on cell performance but also on local energy market dynamics. In future studies, combining this framework with user-dependent load profiles, dynamic operating conditions and real-time electricity pricing will make both design decisions and operational strategies more robust. Furthermore, the model can be extended to evaluate different separator types, new electrolyte formulations and materials that offer higher temperature resistance; such applications will contribute to the development of more competitive AWE systems on both the performance and cost side.

The proposed two-stage framework is not methodologically specific to alkaline water electrolyzers, as it is based on the calculation of electrochemical performance at the cell level and the transfer of this output to technical–economic analysis. In principle, it can be extended to other electrolyzer types such as PEM or AEM. However, the parameterization used in this study is specific to AWE and is based on KOH/NaOH conductivity correlations, separator structural properties and the associated kinetic parameter set. Adapting the framework to PEM or AEM systems requires the appropriate sub-models representing membrane conductivity, moisture management and ion transport processes specific to these technologies.

In future work, it is intended to extend the model to include two-phase flow and gas bubble dynamics, and to represent mass and ohmic losses more realistically, particularly at high current densities. Furthermore, it is planned to apply this developed integrated performance–cost framework comparatively with anion exchange membrane (AEM) electrolyzers.

Author Contributions: Conceptualization, H.O., S.Ç. and B.A.H.; methodology, H.O., S.Ç. and B.A.H.; software, A.E.K. and H.O.; validation, H.O., S.Ç. and B.A.H.; formal analysis, S.Ş.D. and A.E.K.; investigation, S.Ş.D. and A.E.K.; resources, A.E.K. and H.O.; data curation, S.Ş.D. and A.E.K.; writing—original draft preparation, S.Ş.D., A.E.K., H.O., S.Ç. and B.A.H.; writing—review and editing, H.O., S.Ç. and B.A.H.; visualization, A.E.K. and H.O.; supervision, H.O., S.Ç. and B.A.H.; project administration, H.O., S.Ç. and B.A.H.; funding acquisition, H.O., S.Ç. and B.A.H. All authors have read and agreed to the published version of the manuscript.

Funding: This research received no external funding.

Data Availability Statement: The original contributions presented in this study are included in the article. Further inquiries can be directed to the corresponding author.

Acknowledgments: The authors of this work are thankful for the financial support and the analytical software licence provided by Ankara Yildirim Beyazit University and the University of Surrey.

Conflicts of Interest: The authors declare no conflicts of interest.

Nomenclature

The following nomenclatures are used in this manuscript:

Abbreviations	
AWE	Alkaline water electrolyzer
AEM	Anion exchange membrane
CAPEX	Component-level capital expenses
EES	Engineering equation solver
HHV	Higher heating value
LCOH	Levelized cost of hydrogen
LCOE	Levelized cost of electricity
LHV	Lower heating value
OPEX	Operational expenses
PEM	Proton exchange membrane
PPS	Polyphenylene sulphide
PV	Photovoltaic
SMR	Steam methane reforming
SOE	Solid oxide electrolysis
VOC	Volatile organic compounds
Roman Symbols	
H_2	Hydrogen
OH^-	Hydroxide ion
CO_2	Carbon dioxide
NO_x	Nitrogen oxides
KOH	Potassium hydroxide
NaOH	Sodium hydroxide
O_x	Oxidation
Red	Reduction
T	Temperature, °C
U	Voltage, V
I	Current density, A/m^2
C	Concentration
C	Molarity, $mol{\cdot}L^{-1}$
F	Factor
E	Equilibrium potential
Y	Mass fraction of solution, wt%
R	Ohmic losses, $\Omega{\cdot}m^2$
t	Activation overvoltage, $m^2{\cdot}A^{-1}$
S	Activation overvoltage, V
σ	Electrical conductivity, $S{\cdot}m^{-1}$
ρ	Solution density, $kg{\cdot}m^{-3}$
M_w	Molar mass, $g{\cdot}mol^{-1}$
ε	Porosity
τ	Tortuosity
d	Thickness of separator, m
$\varnothing$	Volume fraction
σ	Conductivity
η	Overpotential
R	Universal gas constant
F	Faraday constant
α	Transfer coefficient
F_s	System factor
F_m	Module factor
F_{mn}	Maintenance factor

Subscripts

act	activation
conc	concentration
op	overpotential
ohm	ohmic
H_2	hydrogen
K	KOH
N	NaOH
g	gas
m	module
s	separator
e	effective
0	equilibrium
l	electrolyte
loc	local
c	cathodic
a	anodic

Appendix A

This appendix compiles standard electrochemical expressions and empirical correlations that are only referenced in the main text. The equations provided below have been used to define the fundamental components of cell potential, calculate electrolyte properties and convert intermediate quantities. Equation (A1) provides a basic form of the polarization curve for a described operation temperature [19]:

$$U_{cell} = U_{rev} + r \cdot i + s \cdot \log(t \cdot i + 1) \quad \text{(A1)}$$

In order to simulate the temperature (T) dependence of the overvoltages, an adjustment was made to Equation (1) to include the effect of temperature on the parameters r and t with Equations (A2) and (A3):

$$r = r_1 + r_2 \cdot T \quad \text{(A2)}$$

$$t = t_1 + (t_2/T) + (t_3/T^2) \quad \text{(A3)}$$

In alkaline water electrolysis, the conductivity of the medium is determined by the transport of hydroxide ions in the electrolyte, making KOH and NaOH the most commonly used solutions. The literature indicates that conductivity (σ) is a function of concentration (C) and temperature (T); furthermore, geometric effects such as the electrode–separator gap can be captured by empirical relationships. However, assuming the mass fraction to be independent of temperature and density limits the accuracy in parametric and multi-physics analyses. In this study, a formulation incorporating the effects of T and density was adopted; the σ–T–C correlation for KOH and an equivalent correlation derived from initial experimental data for NaOH were used. The applied empirical models are presented in Equations (A4) and (A5). The KOH and NaOH ionic conductivity relationships used in this study are semi-empirical, multi-term fitting functions developed based on experimental conductivity data reported in the literature. The equations are not closed-form expressions taken directly from a single source, but have been rearranged to represent the conductivity–temperature–concentration trends reported in different studies [57,58]:

$$\sigma_{KOH} = K_1 + K_2 \cdot T + K_3 \cdot {Y_K}^2 + K_4 \cdot {Y_K}^3 + K_5 \cdot T \cdot Y_K \quad \text{(A4)}$$

$$\sigma_{NaOH} = L_1 + L_2 \cdot T + L_3 \cdot {Y_N}^3 + L_4 \cdot {Y_N}^2 + L_5 \cdot Y_N \quad \text{(A5)}$$

where σ is the electrical conductivity of the electrolyte in $S \cdot m^{-1}$, T is the temperature in °C, Y_K is the mass fraction of KOH, Y_N is the mass fraction of NaOH, and K and L are the coefficients for KOH and NaOH, respectively. In specific conductance values, the concentration is usually expressed in two units: percent by weight (Y) and molarity (M). The conversion between these units is described by the following equation (Equation (A6)) [58].

$$C = Y/100 \cdot \rho \cdot {M_w}^{-1} \tag{A6}$$

where Y is the mass fraction of solution (wt%) in the electrolyte, ρ is the solution density of the electrolyte in $kg \cdot m^{-3}$, M_w is the molar mass $g \cdot mol^{-1}$ and C is the molarity in $mol \cdot L^{-1}$ or M. Empirical correlations that relate mass fraction and molarity to density have been developed to determine electrolyte density at specific temperatures and concentrations. The same correlation is used for KOH and NaOH where density is given as a function of the temperature and mass fraction in Equation (A7) and Equation (A8), respectively [61].

$$\rho_K = (P_1 + P_2 \cdot T + P_3 \cdot T^2) \cdot 10^{((P4+P5 \cdot T) \cdot YK))} \tag{A7}$$

$$\rho_N = (R_1 + R_2 \cdot T + R_3 \cdot T^2) \cdot 10^{((R4+R5 \cdot T) \cdot YN))} \tag{A8}$$

The cost figures originally reported for different years were converted to nominal 2024 USD using an inflation adjustment based on a consumer price index (CPI) deflator. The conversion was performed as follows (Equation (A9)):

$$Cost_{2024} = Cost_y \cdot (CPI\_2024/CPI_y) \tag{A9}$$

where $Cost_y$ is the reported cost in year y and CPI_y is the corresponding index value. This normalization ensures consistent comparison of CapEx/OpEx inputs used in Table 4 across all scenarios.

References

1. Megía, P.J.; Vizcaíno, A.J.; Calles, J.A.; Carrero, A. Hydrogen production technologies: From fossil fuels toward renewable sources. A mini review. *Energy Fuels* **2021**, *35*, 16403–16415. [CrossRef]
2. Brockway, P.E.; Owen, A.; Brand-Correa, L.I.; Hardt, L. Estimation of global final-stage energy-return-on-investment for fossil fuels with comparison to renewable energy sources. *Nat. Energy* **2019**, *4*, 612–621. [CrossRef]
3. Shindell, D.; Smith, C.J. Climate and air-quality benefits of a realistic phase-out of fossil fuels. *Nature* **2019**, *573*, 408–411. [CrossRef] [PubMed]
4. Chun, Y.N.; Yang, Y.C.; Yoshikawa, K. Hydrogen generation from biogas reforming using a gliding arc plasma-catalyst reformer. *Catal. Today* **2009**, *148*, 283–289. [CrossRef]
5. Nikolaidis, P.; Poullikkas, A. A comparative overview of hydrogen production processes. *Renew. Sustain. Energy Rev.* **2017**, *67*, 597–611. [CrossRef]
6. El-Shafie, M. Hydrogen production by water electrolysis technologies: A review. *Results Eng.* **2023**, *20*, 101426. [CrossRef]
7. Muazzam, Y.; Yousaf, M.; Zaman, M.; Elkamel, A.; Mahmood, A.; Rizwan, M.; Adnan, M. Thermo-economic analysis of integrated hydrogen, methanol and dimethyl ether production using water electrolyzed hydrogen. *Resources* **2022**, *11*, 85. [CrossRef]
8. Emam, A.S.; Hamdan, M.O.; Abu-Nabah, B.A.; Elnajjar, E. A review on recent trends, challenges, and innovations in alkaline water electrolysis. *Int. J. Hydrogen Energy* **2024**, *64*, 599–625. [CrossRef]
9. Lopez, V.M.; Ziar, H.; Haverkort, J.W.; Zeman, M.; Isabella, O. Dynamic operation of water electrolyzers: A review for applications in photovoltaic systems integration. *Renew. Sustain. Energy Rev.* **2023**, *182*, 113407. [CrossRef]
10. El-Emam, R.S.; Özcan, H. Comprehensive review on the techno-economics of sustainable large-scale clean hydrogen production. *J. Clean. Prod.* **2019**, *220*, 593–609. [CrossRef]
11. Gambou, F.; Guilbert, D.; Zasadzinski, M.; Rafaralahy, H. A comprehensive survey of alkaline electrolyzer modeling: Electrical domain and specific electrolyte conductivity. *Energies* **2022**, *15*, 3452. [CrossRef]
12. Vedrtnam, A.; Kalauni, K.; Pahwa, R. A review of water electrolysis technologies with insights into optimization and numerical simulations. *Int. J. Hydrogen Energy* **2025**, *140*, 694–727. [CrossRef]

13. Grigoriev, S.A.; Fateev, V.N.; Bessarabov, D.G.; Millet, P. Current status, research trends, and challenges in water electrolysis science and technology. *Int. J. Hydrogen Energy* **2020**, *45*, 26036–26058. [CrossRef]
14. Horri, B.A.; Ozcan, H. Green hydrogen production by water electrolysis: Current status and challenges. *Curr. Opin. Green Sustain. Chem.* **2024**, *47*, 100932. [CrossRef]
15. Shih, A.J.; Monteiro, M.C.; Dattila, F.; Pavesi, D.; Philips, M.; da Silva, A.H.; Vos, R.E.; Ojha, K.; Park, S.; van der Heijden, O.; et al. Water electrolysis. *Nat. Rev. Methods Primers* **2022**, *2*, 84. [CrossRef]
16. Hassan, Q.; Sameen, A.Z.; Salman, H.M.; Jaszczur, M. Large-scale green hydrogen production via alkaline water electrolysis using solar and wind energy. *Int. J. Hydrogen Energy* **2023**, *48*, 34299–34315. [CrossRef]
17. Ren, Z.; Wang, J.; Yu, Z.; Zhang, C.; Gao, S.; Wang, P. Experimental studies and modeling of a 250-kW alkaline water electrolyzer for hydrogen production. *J. Power Sources* **2022**, *544*, 231886. [CrossRef]
18. Sánchez, M.; Amores, E.; Rodríguez, L.; Clemente-Jul, C. Semi-empirical model and experimental validation for the performance evaluation of a 15 kW alkaline water electrolyzer. *Int. J. Hydrogen Energy* **2018**, *43*, 20332–20345. [CrossRef]
19. Sánchez, M.; Amores, E.; Abad, D.; Rodríguez, L.; Clemente-Jul, C. Aspen Plus model of an alkaline electrolysis system for hydrogen production. *Int. J. Hydrogen Energy* **2020**, *45*, 3916–3929. [CrossRef]
20. Lee, B.; Lim, D.; Lee, H.; Lim, H. Which water electrolysis technology is appropriate?: Critical insights of potential water electrolysis for green ammonia production. *Renew. Sustain. Energy Rev.* **2021**, *143*, 110963. [CrossRef]
21. Smolinka, T.; Bergmann, H.; Garche, J.; Kusnezoff, M. The history of water electrolysis. In *Electrochemical Power Sources: Fundamentals, Systems, and Applications*; Elsevier: Amsterdam, The Netherlands, 2022; pp. 83–164.
22. Brauns, J.; Turek, T. Alkaline water electrolysis powered by renewable energy: A review. *Processes* **2020**, *8*, 248. [CrossRef]
23. Dreoni, M.; Balduzzi, F.; Ferro, F.M.; Panichi, K.; Ponticorvo, E.; Ferrara, G.; Bianchini, A. Towards a comprehensive, high-fidelity, multi-physics simulation framework for alkaline water electrolyzers. *Int. J. Hydrogen Energy* **2025**, *111*, 238–250. [CrossRef]
24. Zheng, Y.; You, S.; Bindner, H.W.; Münster, M. Optimal day-ahead dispatch of an alkaline electrolyser system concerning thermal–electric properties and state-transitional dynamics. *Appl. Energy* **2022**, *307*, 118091. [CrossRef]
25. Ding, S.; Guo, B.; Hu, S.; Gu, J.; Yang, F.; Li, Y.; Dang, J.; Liu, B.; Ma, J. Analysis of the effect of characteristic parameters and operating conditions on exergy efficiency of alkaline water electrolyzer. *J. Power Sources* **2022**, *537*, 231532. [CrossRef]
26. Dash, S.; Singh, A.; Jose, S.; Vincent Herald Wilson, D.; Elangovan, D.; Surapraraju, S.K.; Natarajan, S.K. Advances in green hydrogen production through alkaline water electrolysis: A comprehensive review. *Int. J. Hydrogen Energy* **2024**, *83*, 614–629. [CrossRef]
27. Chen, Y.; Mojica, F.; Li, G.; Chuang, P.Y.A. Experimental study and analytical modeling of an alkaline water electrolysis cell. *Int. J. Energy Res.* **2017**, *41*, 2365–2373. [CrossRef]
28. Aquigeh, I.N.; Ayissi, M.Z.; Bitondo, D. Multiphysical models for hydrogen production using NaOH and stainless steel electrodes in alkaline electrolysis cell. *J. Combust.* **2021**, *2021*, 6673494. [CrossRef]
29. Kovač, A.; Marciuš, D.; Budin, L. Solar hydrogen production via alkaline water electrolysis. *Int. J. Hydrogen Energy* **2019**, *44*, 9841–9848. [CrossRef]
30. Saleem, M.S.; Abas, N.; Kalair, A.R.; Rauf, S.; Haider, A.; Tahir, M.S.; Sagir, M. Design and optimization of hybrid solar-hydrogen generation system using TRNSYS. *Int. J. Hydrogen Energy* **2020**, *45*, 15814–15830. [CrossRef]
31. Foss, C.E.L.; Svensson, A.M.; Gullbrekken, Ø.; Sunde, S.; Vullum-Bruer, F. Temperature effects on performance of graphite anodes in carbonate based electrolytes for lithium ion batteries. *J. Energy Storage* **2018**, *17*, 395–402. [CrossRef]
32. Al-Mahgari, A.M.; Al-Nimr, M.A.; Khashan, S.A. Pressurized green hydrogen from water electrolysis: Compression before or after electrolysis? A comparison among different configurations. *J. Energy Storage* **2023**, *73*, 109251. [CrossRef]
33. Haoran, C.; Xia, Y.; Wei, W.; Yongzhi, Z.; Bo, Z.; Leiqi, Z. Safety and efficiency problems of hydrogen production from alkaline water electrolyzers driven by renewable energy sources. *Int. J. Hydrogen Energy* **2024**, *54*, 700–712. [CrossRef]
34. Adibi, T.; Sojoudi, A.; Saha, S.C. Modeling of thermal performance of a commercial alkaline electrolyzer supplied with various electrical currents. *Int. J. Thermofluids* **2022**, *13*, 100126. [CrossRef]
35. Wang, T.; Wang, J.; Zhang, C.; Wang, P.; Ren, Z.; Guo, H.; Wu, Z.; Wang, F. Direct operational data-driven workflow for dynamic voltage prediction of commercial alkaline water electrolyzers based on artificial neural network (ANN). *Fuel* **2024**, *376*, 132624. [CrossRef]
36. David, M.; Ocampo-Martínez, C.; Sánchez-Peña, R. Advances in alkaline water electrolyzers: A review. *J. Energy Storage* **2019**, *23*, 392–403. [CrossRef]
37. Rodríguez, J.; Amores, E. CFD modeling and experimental validation of an alkaline water electrolysis cell for hydrogen production. *Processes* **2020**, *8*, 1634. [CrossRef]
38. Hu, K.; Fang, J.; Ai, X.; Huang, D.; Zhong, Z.; Yang, X.; Wang, L. Comparative study of alkaline water electrolysis, proton exchange membrane water electrolysis and solid oxide electrolysis through multiphysics modeling. *Appl. Energy* **2022**, *312*, 118788. [CrossRef]

39. Niroula, S.; Chaudhary, C.; Subedi, A.; Thapa, B.S. Parametric modelling and optimization of alkaline electrolyzer for the production of Green Hydrogen. *IOP Conf. Ser. Mater. Sci. Eng.* **2023**, *1279*, 012005. [CrossRef]
40. Benghanem, M.; Almohamadi, H.; Haddad, S.; Mellit, A.; Chettibi, N. The effect of voltage and electrode types on hydrogen production powered by photovoltaic system using alkaline and PEM electrolyzers. *Int. J. Hydrogen Energy* **2024**, *57*, 625–636. [CrossRef]
41. Kumar, S.S.; Lim, H. An overview of water electrolysis technologies for green hydrogen production. *Energy Rep.* **2022**, *8*, 13793–13813. [CrossRef]
42. Lohmann-Richters, F.P.; Renz, S.; Lehnert, W.; Müller, M.; Carmo, M. Review—Challenges and Opportunities for Increased Current Density in Alkaline Electrolysis by Increasing the Operating Temperature. *J. Electrochem. Soc.* **2021**, *168*, 114501. [CrossRef]
43. Kuckshinrichs, W.; Koj, J.C. Levelized cost of energy from private and social perspectives: The case of improved alkaline water electrolysis. *J. Clean. Prod.* **2018**, *203*, 619–632. [CrossRef]
44. BloombergNEF. Hydrogen Supply Outlook 2024: A Reality Check. Available online: https://about.bnef.com/blog/hydrogen-supply-outlook-2024-a-reality-check (accessed on 8 June 2025).
45. Lee, B.; Lee, H.; Cho, H.S.; Cho, W.C.; Kim, C.H.; Lim, H. Projected economic outlook and scenario analysis for H_2 production by alkaline water electrolysis on the basis of the unit electricity price, the learning rate, and the automation level. *Sustain. Energy Fuels* **2019**, *3*, 1799–1807. [CrossRef]
46. Reksten, A.H.; Thomassen, M.S.; Møller-Holst, S.; Sundseth, K. Projecting the future cost of PEM and alkaline water electrolysers; a CAPEX model including electrolyser plant size and technology development. *Int. J. Hydrogen Energy* **2022**, *47*, 38106–38113. [CrossRef]
47. Zun, M.T.; McLellan, B.C. Cost projection of global green hydrogen production scenarios. *Hydrogen* **2023**, *4*, 932–960. [CrossRef]
48. Sadiq, M.; Alshehhi, R.J.; Urs, R.R.; Mayyas, A.T. Techno-economic analysis of Green-H_2@Scale. *Renew. Energy* **2023**, *219*, 119362. [CrossRef]
49. McPhy. McLyzer Range: 200 to 3200 Nm^3/h at 30 Bar. Available online: https://cellar-c2.services.clever-cloud.com/com-mcphy/uploads/2023/06/2023_McLyzer-Product-Line-EN.pdf (accessed on 2 June 2025).
50. Sunfire. Sunfire-HyLink Alkaline. Available online: https://sunfire.de/en/products/pressurized-alkaline-electrolyzers-ael/ (accessed on 2 June 2025).
51. Hygreen Energy. Alkaline Electrolyzers. Available online: https://www.hygreenenergy.com/electrolyzers/alkaline (accessed on 3 June 2025).
52. Thyssenkrupp Nucera. Green Hydrogen: Alkaline Water Electrolysis Solutions. Available online: https://www.thyssenkrupp-nucera.com/green-hydrogen (accessed on 3 June 2025).
53. De Groot, M.T.; Kraakman, J.; Barros, R.L.G. Optimal operating parameters for advanced alkaline water electrolysis. *Int. J. Hydrogen Energy* **2022**, *47*, 34773–34783. [CrossRef]
54. Xu, X.; Zhao, Z.; Song, C.; Xu, L.; Zhang, W. Seawater membrane distillation coupled with alkaline water electrolysis for hydrogen production: Parameter influence and techno-economic analysis. *Membranes* **2025**, *15*, 60. [CrossRef]
55. Sebbahi, S.; Nabil, N.; Alaoui-Belghiti, A.; Laasri, S.; Rachidi, S.; Hajjaji, A. Assessment of the three most developed water electrolysis technologies: Alkaline Water Electrolysis, Proton Exchange Membrane and Solid-Oxide Electrolysis. *Mater. Today Proc.* **2022**, *66*, 140–145. [CrossRef]
56. Lange, H.; Klose, A.; Lippmann, W.; Urbas, L. Technical evaluation of the flexibility of water electrolysis systems to increase energy flexibility: A review. *Int. J. Hydrogen Energy* **2023**, *48*, 15771–15783. [CrossRef]
57. Le Bideau, D.; Mandin, P.; Benbouzid, M.; Kim, M.; Sellier, M. Review of necessary thermophysical properties and their sensivities with temperature and electrolyte mass fractions for alkaline water electrolysis multiphysics modelling. *Int. J. Hydrogen Energy* **2019**, *44*, 4553–4569. [CrossRef]
58. Al-Salih, H.; Abu-Lebdeh, Y. Investigating the phase diagram-ionic conductivity isotherms relationship in aqueous solutions of strong bases: Lithium, sodium and potassium hydroxides. *J. Mol. Liq.* **2025**, *422*, 127179. [CrossRef]
59. Shangguan, Z.; Li, H.; Yang, B.; Zhao, Z.; Wang, T.; Jin, L.; Zhang, C. Optimization of alkaline electrolyzer operation in renewable energy power systems: A universal modeling approach for enhanced hydrogen production efficiency and cost-effectiveness. *Int. J. Hydrogen Energy* **2024**, *49*, 943–954. [CrossRef]
60. van der Does, W.L.; Valle, N.; Haverkort, J.W. Multiphase alkaline water electrolysis simulations: The need for a solid pressure model to explain experimental bubble overpotentials. *Int. J. Hydrogen Energy* **2025**, *102*, 295–303. [CrossRef]
61. Remme, U. *Global Hydrogen Review 2024*; IEA: Paris, France, 2024.
62. Clean Hydrogen Observatory. Alkaline Electrolyser Cost. 2024. Available online: https://observatory.clean-hydrogen.europa.eu/hydrogen-landscape/production-trade-and-cost/electrolyser-cost (accessed on 8 June 2025).
63. Hydrogen Council. *Hydrogen Insights 2022*; Hydrogen Council: Brussels, Belgium, 2022.
64. IRENA. *Green Hydrogen Strategy: A Guide to Design*; IRENA: Abu Dhabi, United Arab Emirates, 2024.

https://doi.org/10.3390/en19030835

65. Agora Industry. EU Map of Hydrogen Production Costs (Documentation 2024). Available online: https://www.agora-industry.org/data-tools/agoras-eu-map-of-hydrogen-production-costs (accessed on 8 June 2025).
66. Krishnan, S.; Koning, V.; de Groot, M.T.; de Groot, A.; Mendoza, P.G.; Junginger, M.; Kramer, G.J. Present and future cost of alkaline and PEM electrolyser stacks. *Int. J. Hydrogen Energy* **2023**, *48*, 32313–32330. [CrossRef]
67. Ginsberg, M.J.; Venkatraman, M.; Esposito, D.V.; Fthenakis, V.M. Minimizing the cost of hydrogen production through dynamic polymer electrolyte membrane electrolyzer operation. *Cell Rep. Phys. Sci.* **2022**, *3*, 100935. [CrossRef]
68. Morgan, E.R.; Manwell, J.F.; McGowan, J.G. Opportunities for economies of scale with alkaline electrolyzers. *Int. J. Hydrogen Energy* **2013**, *38*, 15903–15909. [CrossRef]
69. Rodríguez, J.; Palmas, S.; Sánchez-Molina, M.; Amores, E.; Mais, L.; Campana, R. Simple and precise approach for determination of ohmic contribution of diaphragms in alkaline water electrolysis. *Membranes* **2019**, *9*, 129. [CrossRef]
70. Haverkort, J.W.; Rajaei, H. Voltage losses in zero-gap alkaline water electrolysis. *J. Power Sources* **2021**, *497*, 229864. [CrossRef]
71. Hoang, A.L.; Balakrishnan, S.; Hodges, A.; Tsekouras, G.; Al-Musawi, A.; Wagner, K.; Lee, C.-Y.; Swiegers, G.F.; Wallace, G.G. High-performing catalysts for energy-efficient commercial alkaline water electrolysis. *Sustain. Energy Fuels* **2023**, *7*, 31–60. [CrossRef]
72. Cozzolino, R.; Bella, G. A review of electrolyzer-based systems providing grid ancillary services: Current status, market, challenges and future directions. *Front. Energy Res.* **2024**, *12*, 1358333. [CrossRef]

https://doi.org/10.3390/en19030835